

TEXAS A&M UNIVERSITY
MECHANICAL ENGINEERING DEPARTMENT
TURBOMACHINERY LABORATORY
TRIBOLOGY GROUP

A Thermo-Elasto-Hydrodynamic (TEHD) Computational
Analysis of Tilting Pad Thrust Bearings: Analytical and FE
Pad Structure Models

Research Progress Report to the TAMU Turbomachinery Research
Consortium

TRC-B&C-01-18

By

Luis San Andrés
Mast-Childs Chair Professor
Principal Investigator

Rasool Koosha
Graduate Research Assistant

May 2018

EXECUTIVE SUMMARY

Work in 2018 extends an earlier (2017) single-pad, laminar flow thermohydrodynamic (THD) model, into a multiple-pad, turbulent flow thermoelastohydrodynamic (TEHD) model for the prediction of the static and dynamic force performance of tilting pad thrust bearings (TPTBs). The updated XLTHRUSTBEARINGR[®] software offers three ways, simple to complex, to account for mechanical and thermal pad deformations in the analysis. The first way relies on an approximate solution, based on a generalization of the EulerBernoulli beam theory, and outputs the axial deformation field on a pad top surface. The second method is an in-house three dimensional (3D) Finite Element (FE) model that accounts for all modes of elastic deformations, both pressure and temperature induced, and delivers a complete 3D pad deformation field. The third method, specific for pads with a complex geometry, provides a user with the option to model the pad in a commercial FE software and to import the (reduced) stiffness matrix into the code. This method only accounts for pad mechanical deformations and produces axial deformations of the pad top surface.

Predictions of pad sub-surface temperature are benchmarked against published test data for an eight-pad TPTB, 267 mm in OD, operating from 4 krpm to 13 krpm (maximum surface speed = 54 to 181 m/s) and under a specific load/pad ranging from 0.69 to 3.44 MPa. The test data covers operation in the laminar flow, turbulent flow and transition flow regimes. Predictions agree with measured temperatures for most test conditions, including the transition flow regime.

NOMENCLATURE

| | |
|-----------------|---|
| A_i | Weight coefficients for pad analytical model [m] |
| c_p | Lubricant specific heat [J/kg °C] |
| C_{XY} | Damping coefficients ($X = z, x, y, \eta, \gamma, \xi$ and $Y = e_c, \phi, \psi, e_p, \alpha, \beta$) |
| e_c | Thrust collar axial location [m] |
| e_p | Pivot tip axial location [m] |
| E | Elasticity modulus [Pa] |
| f_i | Dimensionless shape functions for pad analytical model |
| h | Fluid film thickness [m] |
| K_{XY} | Stiffness coefficients ($X = z, x, y, \eta, \gamma, \xi$ and $Y = e_c, \phi, \psi, e_p, \alpha, \beta$) |
| N | Shaft rotational speed [rpm], $N = \Omega\pi/30$ |
| N_j | Finite Element shape functions |
| N_P | Number of pads in a bearing [-] |
| m_r, m_θ | Gradient radial and circumferential loading on the pad [Nm] |
| M_r, M_θ | Radial and circumferential moments on the pad [Nm] |
| P | Pressure [N/m ²] |
| Re | Local circumferential Reynolds Number, $Re = \frac{R\Omega\rho h}{\mu}$ |
| R_i, R_o | Inner radius and outer radius of a pad [m] |
| R_P, θ_P | Pivot radial and circumferential location [m] |
| t | Time [s] |
| t_P | Pad thickness [m] |
| T | Temperature [°C] |
| U, V, W | Radial, circumferential, and axial components of the fluid velocity [m/s] |
| V_B | Bending Energy of a pad [J] |
| w | Pad top surface axial displacement [m] |

| | |
|--------------------------|---|
| W_M | Mechanical loading energy [J] |
| W_T | Thermal loading energy [J] |
| W_z | Axial load applied on the bearing [N] |
| Z_{XY} | Stiffness coefficients ($X = z, x, y, \eta, \gamma, \xi$ and $Y = e_c, \phi, \psi, e_p, \alpha, \beta$) |
| α, β | Pad tilt angles around (γ, ξ) axes, respectively [rad] |
| α_{TV} | Lubricant viscosity-temperature coefficient [$1/^\circ\text{C}$] |
| α_T | Thermal expansion coefficient [$1/^\circ\text{C}$] |
| ϵ_m, ϵ_H | Eddy viscosity for momentum and heat transfer [m^2/s] |
| θ_l, θ_t | Circumferential location of leading edge and trailing edge [rad] |
| λ | Heat convection coefficient [$\text{W}/\text{m}^2\text{C}$] |
| μ | Lubricant dynamic viscosity [Pa.s] |
| ϕ, ψ | Thrust Collar Misalignment angles around (x, y) axes, respectively [rad] |
| ν | Lubricant kinematic viscosity [cSt] |
| ρ | Lubricant density [kg/m^3] |
| κ | Lubricant conductivity coefficient [$\text{W}/\text{m C}$] |
| κ_P | Pad material conductivity coefficient [$\text{W}/\text{m C}$] |
| ω | Excitation frequency [rad/s] |
| Ω | Shaft angular speed [rad/s] |

Matrices and Vectors

| | |
|----------------------------|---|
| C | Damping coefficient matrix |
| F_B | Body force vector (gravity or magnetic) |
| K | Stiffness coefficient matrix |
| M | Complex stiffness coefficient matrix |
| u | Displacement vector |
| σ | Stress tensor [Pa] |

ε Strain tensor [m/m]

Subscripts

F Fluid film

i Inner radius

l Leading edge

o Outer radius

p Pivot

P Pad

t Trailing edge

Su Lubricant supply condition

Abbreviations

FEM Finite Element Method

FDM Finite Difference Method

ID Inner Diameter

OD Outer Diameter

TEHD Thermo-elasto-hydrodynamic, includes pressure and thermally induced deformations

THD Thermo-hydrodynamic

TPTB Tilting Pad Thrust Bearing

CONTENTS

| | |
|--|----|
| 1. Introduction | 1 |
| 2. Review of past work | 4 |
| 3. Analysis | 7 |
| 3.1. Reynolds Equation for a Thin Film | 8 |
| 3.2. The Fluid Flow Thermal Energy Transport Equation | 8 |
| 3.3. The Heat Conduction Equation in a Pad | 9 |
| 3.4. Elasticity Analysis for Pad Deformations | 9 |
| 3.4.1. Finite Element Model for Pad Elastic Deformations | 9 |
| 3.4.2. Analytical Solution for Pad Elastic Deformations | 11 |
| 3.4.3. Substructuring Analysis for Pad Mechanical Deformations (Reduction of DOFs) | 12 |
| 4. Validation of the Analytical Solution and FE Model for Pad Deformations | 14 |
| 4.1. Validations of pad axial deformations for a cylindrical pivot TPTB | 14 |
| 4.2. Validations of pad axial deformations for a spherical pivot TPTB | 18 |
| 5. Comparison Of Predictions Versus Test Data | 22 |
| Closure | 30 |
| References | 32 |
| A. Appendix: Turbulent Flow Functions | 33 |
| B. Shape Functions for an Analytical Solution of Pad Elastic Deformations | 36 |

LIST OF FIGURES

| | | |
|-----|--|----|
| 1. | Schematic view of a tilting pad thrust bearing (Film thickness and pad tilts exaggerated). | 1 |
| 2. | Schematic deformations of pads and thrust collar in a TPTB (not to scale). | 2 |
| 3. | Geometry and coordinate systems for a TPTB. | 7 |
| 4. | Schematic view of heat conduction to the bearing elements (pads and thrust collar) and heat advection by the fluid. | 8 |
| 5. | A schematic view of a cylindrical pivot pad in Guo et al.[20]. (Not to scale) | 14 |
| 6. | : (a) Pad model and boundary conditions at pivot in ANSYS [®] , (b) temperature distribution in pad, (c) hydrodynamic pressure field acting on pad, and (d) contour of pad axial deformations (μm). Results for cylindrical pivot pad taken from Ref.[20], rotor speed = 3 krpm, applied specific load = 1 MPa, supply temperature = 20°C. Cylindrical pivot taken from Ref.[20] | 16 |
| 7. | Axial deformations (μm) on top surface of pad due to combined action of pressure and temperature as obtained by (b) ANSYS [®] , (c) an analytical solution, (d) an in-house FE model. Results for cylindrical pivot pad in Ref.[20], rotor speed = 3 krpm, applied specific load = 1 MPa, supply temperature = 20°C. | 17 |
| 8. | A schematic view of a spherical pivot pad in Mikula [20]. (Not to scale) . | 19 |
| 9. | : (a) Pad model and boundary conditions at pivot in ANSYS [®] , (b) temperature distribution in pad, (c) hydrodynamic pressure field acting on pad, and (d) contour of pad axial deformations (μm). Results for cylindrical pivot pad taken from Ref.[20], rotor speed = 3 krpm, applied specific load = 1 MPa, supply temperature = 46°C. | 20 |
| 10. | Axial deformations (μm) on top surface of pad due to combined action of pressure and temperature as obtained by (b) ANSYS [®] , (c) an analytical solution, (d) a FE model. Results for spherical pivot pad in Ref.[20], rotor speed = 3 krpm, applied specific load = 1 MPa, supply temperature = 46°C. | 21 |
| 11. | Schematic view of a test rig in Mikula [21] to evaluate the operating characteristics of laminar and turbulent flow TPTBs. | 22 |
| 12. | Schematic view of pad and location of thermocouples placed under top surface. Details taken from [21] | 24 |
| 13. | Circumferential Reynolds number at minimum film thickness. (Supply temperature = 46°C, rotor speed = 4 krpm, laminar flow condition) | 25 |
| 14. | Pad subsurface temperature rise versus specific load at pad (a) leading edge and (b) trailing edge. Test data from Ref.[21] versus predictions from the current TEHD model: analytical solution and an in-house FE method. (Supply temperature = 46°C, rotor speed = 4 krpm, laminar flow condition) | 25 |
| 15. | Circumferential Reynolds number at the minimum film thickness. (Supply temperature = 46°C, rotor speed = 10 krpm, turbulent flow condition) . . | 26 |

| | | |
|-----|---|----|
| 16. | TEHD predictions versus measurements for pad subsurface temperature rise versus specific load at pad (a) leading edge and (b) trailing edge using an analytical solution and a FE model. Test data from Ref.[21]. (Supply temperature = 46°C , rotor speed = 10 krpm, turbulent flow condition) . . . | 27 |
| 17. | Laminar flow and turbulent flow predictions versus measurements for pad subsurface temperature rise at pad (a) leading edge and (b) trailing edge. Test data from Ref.[21]. (Supply temperature = 46°C, rotor speed = 10 krpm, turbulent flow condition) | 27 |
| 18. | Circumferential Reynolds number at the minimum film thickness. (Supply temperature = 46°C , specific load = 3.44 MPa) | 28 |
| 19. | TEHD predictions and measured pad subsurface temperature rise versus rotor speed at pad (a) leading edge and (b) trailing edge. Test data from Ref.[21]. (Supply temperature = 46°C , specific load = 3.44 MPa) | 29 |
| 20. | Turbulent flow and laminar flow predictions versus measurements for pad subsurface temperature rise for pad (a) leading edge and (b) trailing edge. Test data from Ref.[21]. (Supply temperature = 46°C, specific load = 3.44 MPa) | 29 |
| 21. | The global (r, θ) and local (r_c, θ_c) cylindrical coordinates systems of a pad. | 37 |

1. INTRODUCTION

Tilting Pad Thrust Bearings (TPTBs), used in rotating machinery to control rotor axial placement, offer advantages such as low power loss, simple installation, and low-cost maintenance. Figure 1 depicts a schematic view of a TPTB (the fluid film thickness and pad tilts are exaggerated for clarity), consisting of a bearing housing, a thrust collar attached to the rotating shaft, and a series of pads supported on pivots. The ports in the bearing housing supply cold lubricant into the bearing pads, meanwhile some hot lubricant leaves the bearing through its sides. In the grooves between pads, the cold supplied lubricant mixes with the upstream hot flow and enters the leading edge of the downstream pad. As the thrust collar rotates, it draws the fluid into the wedge (between a pad and the thrust collar) to generate a hydrodynamic pressure field. Lubricant is sheared through the hydrodynamic wedge and its temperature increases. The load capacity of a hydrodynamic fluid film bearing largely depends on the lubricant viscosity, a function of its temperature[1].

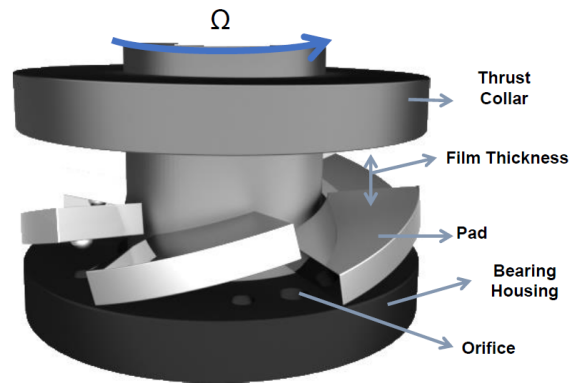


Figure 1: Schematic view of a tilting pad thrust bearing (Film thickness and pad tilts exaggerated).

As Figure 2 shows, thermally and mechanically induced elastic deformations of pads and the thrust collar shape the operating fluid film thickness to impact the static and dynamic force performance of a TPTB [2, 3]. The hydrodynamic pressure acting on a pad warps it backwards around the support point (pivot point) and produces a larger fluid film thickness at its edges. The same pressure also acts on the thrust collar and bends it to enlarge the fluid film thickness, more significantly at the outer radius of a pad. At the same time, a portion of the heat generated in the fluid film is transferred away through bearing elements, creating a temperature gradient which further adds to the deformations

in both the pads and the thrust collar [4, 5]. Ahmed et al [6] studied the characteristic performance of an eight-pad TB with 200 mm in outer diameter (OD) and observe the significance of deformations in pads and the thrust collar specially under a heavy specific load¹, thus proving them vital for accurate modeling.

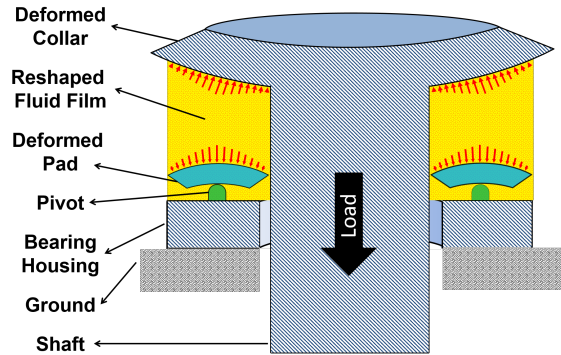


Figure 2: Schematic deformations of pads and thrust collar in a TPTB (not to scale).

Last year TRC report [7] details a thermohydrodynamic model for tilting pad thrust bearings (TPTBs). The model couples a generalized Reynolds equation for the film pressure, including cross-film viscosity variation and turbulence flow effects, a 3D energy transport equation for the film temperature, and a heat conduction equation for pad temperature. A numerical solution of these equations with boundary conditions delivers pressure and temperature fields towards the calculation of the TPTB load capacity, shear drag power loss, and flow rate. A small amplitude thrust collar motions (perturbation) analysis produces first-order pressure fields to calculate the bearing axial stiffness and damping coefficients (frequency reduced). Predictions of film pressure and pad surface temperature agree with archival test data for a laminar flow six-pad TPTB (228 mm OD) under specific load 0.5 to 2.0 MPa and operating with rotor speed 1.5 to 3.0 krpm (36 m/s). Comparisons between predictions and test data show a difference of 8% in peak pressure and 17% for pad temperature.

The present report describes a thermo-elastic-hydrodynamic (TEHD) model that offers three methods to include pad mechanical and thermal elastic deformations. The first is a 3D Finite Element (FE) model which accounts for elastic deformations due to a pad temperature gradient an/or a hydrodynamic pressure field. The modes of elastic deformation in a pad are compression/expansion and bending. The FE model delivers an accurate 3D

¹Unit load or specific load = W_z/A_P , where W_z is the axial load on a pad and A_P is its area.

deformation field (axial, radial, and circumferential) for the entire pad geometry. The second method is an analytical solution that accounts for bending mode deformations, both thermally and mechanically induced, and is based on the EulerBernoulli beam theory that produces an axial displacement field only over a pad top surface. The main advantage of the analytical solution is its fast computational process, albeit with a lesser accuracy than that from the FE model. The third method is specific for pads with a complex geometry and provides the user an option to model a pad in a commercial FE software (ANSYS) and imports the stiffness matrix into the current model. The third method only accounts for pad mechanical deformations and delivers an axial deformation field over a pad top surface.

This report describes a multiple-pad computational analysis tool for the static and dynamic force performance of tilting pad thrust bearings (TPTBs). Unlike single pad models, a multiple-pad predictive tool extends the analysis to include thrust collar misalignment and delivers more realistic predictions. The model performs a single pad analysis if thrust collar is not misaligned to insure an efficient computation process. A 3D thermal energy transport equation in the fluid film, coupled with heat conduction equations in the pads, is solved collectively with a generalized Reynolds equation. That allows for cross-film viscosity variations. Then, the predicted pressure field and temperature rise are employed by an elasticity model to deliver axial elastic deformations for pads.

2. REVIEW OF PAST WORK

Since 1960s, several researchers study the impacts of pad elastic deformations on the performance predictions of tilting pad bearings . However, each researcher has perused a different approach in the calculation of pad elastic deformation. Table 1 highlight the characteristics of each approach. The following describes the advantages and disadvantages associated with each of them.

Table 1: Characteristics of different approaches for the calculation of pad elastic deformations.

| | | | | | |
|-------------------|----------------------|------------------------|--------------------------------------|--------------------------------------|--------------------------------------|
| Researcher | Strenlicht et al.[8] | Robinson [9] | Brochette et al.[10] | Glavatskih et al.[11] | Ahmed et al.[6] |
| Year | 1961 | 1975 | 1996 | 2001 | 2010 |
| Analysis | Euler-Bernouli | Timoshenko | Finite Element | Finite Element | Finite Element |
| Deformation Modes | Bending | Bending Compression | Bending, Compression Expansion | Bending, Compression Expansion | Bending, Compression Expansion |
| Bearing Element | Pads | Pads Collar | Pads Collar | Pads Liner | Pads Collar |

In 1961, Sternlicht et al. [8] are among the first to account for bending deformation of the a pad in the analysis of TPTBs, using the Euler Bernoulli deformation theory. An elasticity equation, integrated over a pad volume using the principle of minimum energy, leads to an analytical solution for axial deformations, both thermally (temperature gradient) and mechanically (hydrodynamic pressure) induced. Sternlicht et al. assume the temperature variation in a pad is linear, hence replacing it with an equivalent mechanical loading. The authors detail predictions for a centrally pivoted TPTB with 0.787 m in OD operating at 320 rpm ($\Omega R_o=13.17$ m/s) and with a minimum film thickness of 25 μm . Compared to the thermo-hydrodynamic (THD) analysis, the thermo-elasto-hydrodynamic (TEHD) analysis (including pad mechanical deformations) predicts a lesser film temperature (up to 25%) and a larger load capacity (42%). Strenlicht et al.'s approach only accounts for the bending mode of deformations (compression/expansion neglected) and is limited to a point pivot TPTB (not applicable for line pivot TPTBs).

In 1975, Robinson and Cameron [9] extend the elastic analysis in TPTBs to include

thermally and mechanically induced deformations of the thrust collar. They also advance their model to account for direct compression caused by mechanical loading and expansion due to thermal loading, using a Timoshenko deformation theory (first order shear deformations are included). In a second part, Robinson and Cameron [12] compare predictions against test data for a three-pad line pivot TPTB with 97 mm in OD operating at rotor speed ranging from 2 to 6 krpm ($\Omega R_o=6.8-20.41$ m/s) and under specific load between 1.37 to 6.89 MPa. Predictions show a very good agreement with measurements with a maximum difference of 9% for the fluid outlet temperature and 8% for the fluid film thickness. In general, the Robinson and Cameron approach can not be used for complex geometries and is widely dependent on measurements.

In 1996, Brockett et al. [10] develop a thermo-elasto-hydrodynamic (TEHD) model for laminar flow fixed geometry thrust bearings. A FE model is incorporated to calculate the elastic deformations: 3D deformation field in pads, both mechanically and thermally induced, and axisymmetric deformation field in the thrust collar, only mechanically induced. Predictions are detailed for a six-pad TB with 0.305 m in OD, operating at a rotor speed of 2 krpm ($\Omega R_m=32$ m/s) and under a specific load between 1.32 to 10.52 MPa. Comparing predictions obtained with and without accounting for elastic deformations in a pad shows that mechanical deformation is small (8% of h_{min}) and leads to a maximum temperature rise of 2°C whereas thermal deformation is relatively large (45% of h_{min}) and could cause a maximum temperature rise up to 24°C. Power loss and flow rate are insignificantly (at most, %8) affected by deformation modes. Predictions of the presented TEHD analysis are not compared against experimental data.

In 2001, Glavatskih and Fillon [11] extend their earlier model (THD model of Ref. [4]) to account for both pressure and temperature induced elastic deformations of pads in a laminar flow TPTBs using a FE model. Predictions are compared against test data for the a six-pad TPTB with 228 mm in OD operating with a rotor speed up to 3 krpm ($\Omega R_o=36$ m/s), and under a specific load up to 2.0 MPa. TEHD predictions for pad temperature show up to 15% improvement over predictions delivered by THD analysis. Three years later, Glavatskih and Fillon [13] expand their TEHD model to include the effects of pad face coating (liner) in the laminar flow TPTB's analysis. Deformations of a pad backing part, thermally and mechanically induced, are calculated through a FE model. For mechanically induced axial deformations in a liner layer, the authors adopt an analytical model from Ref. [14]. Measured pad temperature and fluid film thickness are compared against TEHD and THD predictions. TEHD predictions of fluid film thickness are significantly more accurate

(up to 15%) over predictions obtained using THD analysis.

In 2010, Ahmed et al. [6] use a TEHD analysis tool to study the impact of the elastic deformations of pads and the thrust collar on the performance of a fixed-geometry hydrodynamic TB. Their model accounts for pad deformations due to both pressure and temperature changes and the thrust collar deformations only pressure induced. Predictions for an eight-pad thrust bearing with 200 mm in OD, operating with a rotor speed of 2.6 krpm ($\Omega R_o=27$ m/s), and under a specific load of 1.4 MPa, shows that pad mechanical deformations do not exceed $5 \mu\text{m}$ and have a very limited influence on the fluid film thickness. On the other hand, the pressure induced deformations in the thrust collar raise up to $45 \mu\text{m}$ and significantly influence the film thickness. The predictions made by the TEHD model largely differ from THD predictions as the applied load increases (>0.9 MPa). The maximum difference is 8% for pressure (0.4 MPa), 40% for film thickness ($15 \mu\text{m}$), and 20% for fluid film temperature rise (6°C).

The literature review elaborate on the importance of accounting for pad elastic deformations in the analysis of TPTBs. Among the different approaches used, the analytical solutions are simple and fast albeit offering lesser accuracy than that from a computational physical (FE) models. In addition, the FE analysis can be used for pads of physical complex geometry.

3. ANALYSIS

A brief description of the thermoelastohydrodynamic (TEHD) analysis for TPTBs follows, detailed for multiple-pad analysis including (potential) thrust collar misalignment.

Figure 3 depicts a TPTB geometry and the definition of variables. A global cylindrical coordinate system (r, θ, z) has its origin at the center of bearing housing surface (OB) with the z -axis normal to its surface. Parameters (ϕ, ψ) represent thrust collar misalignment angles around x -axis and y -axis, respectively.

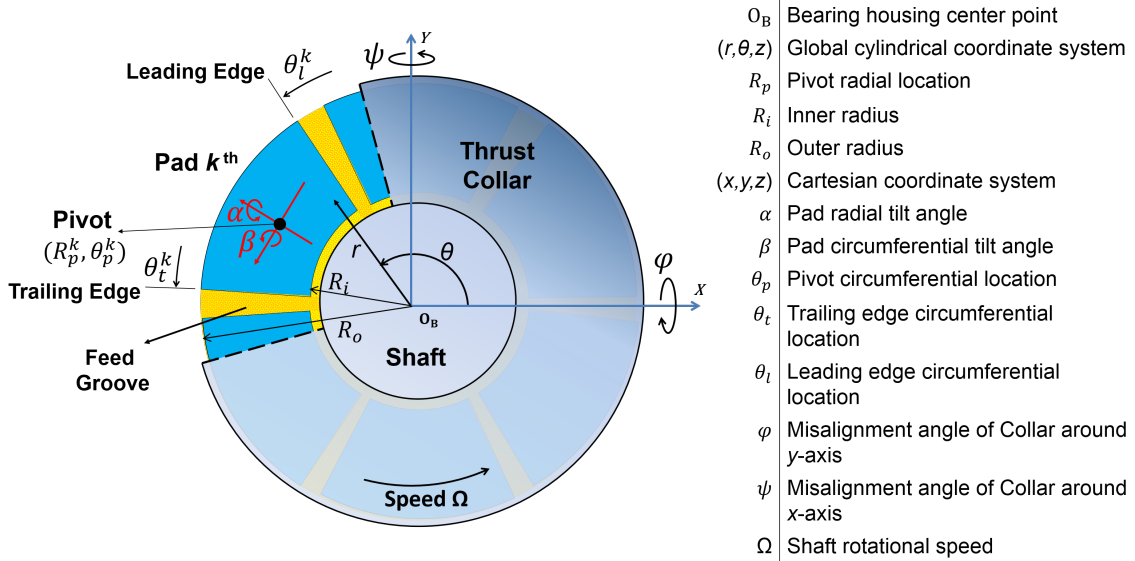


Figure 3: Geometry and coordinate systems for a TPTB.

At any point on a pad surface, the film thickness $(h_{(r, \theta, t)})$ is a function of the thrust collar axial location $(e_{c(t)})$, the pivot axial location $(e_{P(t)})$, and the pad tilt angles $(\alpha_{(t)}, \beta_{(t)})$, respectively around the (γ, ζ) axes. On pad k^{th} with a pivot located at (R_p^k, θ_p^k) , the film thickness is,

$$h_{(r, \theta, t)}^k = (e_c - e_p^k - t_p) + (\phi r) \sin \theta - (\psi r) \cos \theta + (\alpha^k r) \sin(\theta_p^k - \theta) + (\beta^k r) \cos(\theta_p^k - \theta) - (\beta^k R_p^k) \quad \theta_l^k < \theta < \theta_t^k \quad (1)$$

where t_p is the pad thickness. If the thrust collar is perfectly aligned, then $\phi = \psi = 0$ and all pads produce an identical fluid film geometry.

3.1. REYNOLDS EQUATION FOR A THIN FILM

Jeng et al. [15] derive a general form of the Reynolds equation governing the generation of hydrodynamic pressure field ($P_{(r,\theta,t)}$) in a turbulent flow fluid film bearing. The fluid is Newtonian, incompressible, and inertialess. This equation is [15]

$$\frac{1}{r} \frac{\partial}{\partial r} \left(r H_r \frac{\partial P}{\partial r} \right) + \frac{1}{r} \frac{\partial}{\partial \theta} \left(H_\theta \frac{1}{r} \frac{\partial P}{\partial \theta} \right) = \Omega \frac{\partial G}{\partial \theta} + \frac{\partial h}{\partial t} \quad (2)$$

where Ω is the rotor (thrust collar) speed, and (H_r , H_θ , and G) are turbulent flow functions. See Appendix A for the description of the turbulent flow functions.

Note that, in a laminar flow with constant viscosity cross the film,

$$H_r = H_\theta = \frac{h^3}{12\mu}, \quad G = \frac{h}{2} \quad (3)$$

Then, the Reynolds equation takes a familiar form,

$$\frac{1}{r} \frac{\partial}{\partial r} \left(r \frac{h^3}{12\mu} \frac{\partial P}{\partial r} \right) + \frac{1}{r} \frac{\partial}{\partial \theta} \left(\frac{h^3}{12\mu r} \frac{\partial P}{\partial \theta} \right) = \frac{\Omega}{2} \frac{\partial h}{\partial \theta} + \frac{\partial h}{\partial t} \quad (4)$$

3.2. THE FLUID FLOW THERMAL ENERGY TRANSPORT EQUATION

The thermal energy transport equation balances the energy generated due to viscous shear dissipation in the fluid film and the energy disposed through fluid flow advection and conduction to the solids (pads and thrust collar). Figure 4 shows a schematic view of the fluid film boundary conditions.

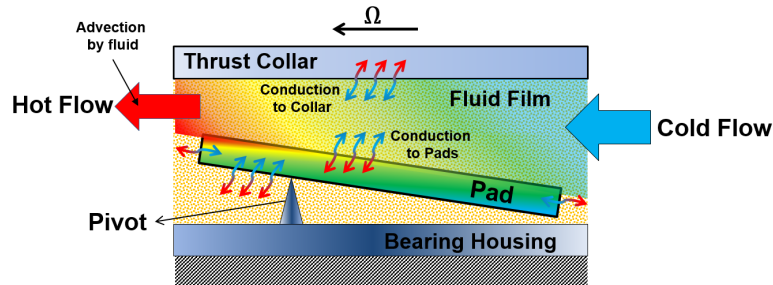


Figure 4: Schematic view of heat conduction to the bearing elements (pads and thrust collar) and heat advection by the fluid.

At a steady state condition, Jeng et al. [15] state the thermal energy transport equation of an incompressible fluid with temperature $T_{(r,\theta,z)}$, as

$$\begin{aligned} \rho c_p \left[U \frac{\partial T}{\partial r} + V \frac{\partial T}{r \partial \theta} + W \frac{\partial T}{\partial z} \right] &= \kappa^* [\nabla^2 T] + \Phi \\ &= \kappa^* \left[\frac{1}{r} \frac{\partial}{\partial r} \left(r \frac{\partial T}{\partial r} \right) + \frac{1}{r^2} \frac{\partial T^2}{r \partial \theta^2} + \frac{\partial T^2}{\partial z^2} \right] + \mu^* \left[\left(\frac{\partial U}{\partial z} \right)^2 + \left(\frac{\partial V}{\partial z} \right)^2 \right] \end{aligned} \quad (5)$$

where ρ and c_p are the lubricant density and specific heat. These parameters are assumed constant over the flow domain. U , V , and W are fluid velocity components in the radial, circumferential, and axial directions, respectively. Above μ^* and κ^* are the turbulent flow viscosity and the turbulent flow heat conductivity, both detailed in Appendix A.

3.3. THE HEAT CONDUCTION EQUATION IN A PAD

The steady-state heat conduction equation governing the flow of heat through a pad with isotropic conductivity is [4],

$$\nabla^2 T_P = \frac{1}{r} \frac{\partial}{\partial r} \left(r \frac{\partial T_P}{\partial r} \right) + \frac{1}{r^2} \frac{\partial T_P^2}{r \partial \theta^2} + \frac{\partial T_P^2}{\partial z^2} = 0 \quad (6)$$

where T_P is the temperature in a pad.

3.4. ELASTICITY ANALYSIS FOR PAD DEFORMATIONS

3.4.1. Finite Element Model for Pad Elastic Deformations

The elastic deformation in a pad is governed by a force equilibrium equation, a strain-displacements equation, and a material constitutive law. Let σ represent the stress tensor in a cylindrical coordinates system; then a solid subject to body force $\mathbf{F}_B = \{F_r, F_\theta, F_z\}^T$ is in equilibrium [10],

$$\mathbf{D}_\sigma^T \sigma + \mathbf{F}_B = 0 \quad (7)$$

where \mathbf{D}_σ is the stress gradient operator for the cylindrical coordinate (r, θ, z) . The thermoelastic law [11] correlates the stress components to any initial, thermal or mechanical strain tensors,

$$\varepsilon_{ij} = \frac{1 + \nu}{E} \sigma_{ij} - \left(\frac{\nu}{E} \sigma_{kk} + \alpha_T \Delta T_P \right) \delta_{ij} \quad i, j, k = r, \theta, z \quad (8)$$

where ε_{ij} is the strain tensor for a material, ν and E are the Poisson ratio and elasticity modulus, α_T is the coefficient of thermal expansion, and ΔT_P represents the temperature variation at each material point, relative to a reference temperature. $\delta_{ij} = \text{zero}$ for $i \neq j$ and unity for $i = j$. A strain-displacement equation [10] relates the strain tensor to a displacement vector \mathbf{u} for each point,

$$\boldsymbol{\varepsilon} = \mathbf{D}_u \mathbf{u} \quad (9)$$

with \mathbf{D}_u as the displacement gradient operator in the cylindrical coordinate system

The principle of virtual works combines the elasticity equations Eqns. (7-9) along with boundary conditions into a single equation, [16]

$$\iiint_V \delta \mathbf{u}^T [\mathbf{D}_u^T \mathbf{E} \mathbf{D}_u \mathbf{u} - \mathbf{D}_u^T \mathbf{E} \Delta T_P \alpha_T - \mathbf{F}_B] dV - \iint_S \delta \mathbf{u}^T \mathbf{P} dS = 0 \quad (10)$$

where \mathbf{P} is the pressure vector acting on a surface. Using shape functions ($N_i, i = 1, \dots, N_{NE}$: number of nodes per element) associated with the FE model, Eqn. (10) becomes a liner system of equations for each element,

$$\mathbf{K}^j \mathbf{u} = \mathbf{f}_B^j + \mathbf{f}_P^j + \mathbf{f}_T^j, \quad j = 1, \dots, N_E : \text{number of elements} \quad (11)$$

where \mathbf{f}_B^j is the body force vector (gravity or magnetic), \mathbf{f}_T^j is the force vector induced due to the temperature gradient, and \mathbf{f}_P^j is induced due to the hydrodynamic pressure on a pad top surface. The local stiffness matrix and load vectors for each element are,

$$\mathbf{K}^j = \iiint_V \mathbf{N}^T \mathbf{D}_u^T \mathbf{E} \mathbf{D}_u \mathbf{N} dV \quad (12a)$$

$$\mathbf{f}_B^j = \iiint_V \mathbf{N}^T \mathbf{F}_B dV, \quad \mathbf{f}_T^j = \iiint_V \mathbf{N}^T \mathbf{D}_u^T \mathbf{E} \mathbf{D}_u \mathbf{N} dV, \quad \mathbf{f}_P^j = \iint_S \mathbf{N}^T \mathbf{P} dS \quad (12b)$$

Thus, the local stiffness matrices and load vectors are stored in a global stiffness matrix \mathbf{K}^G and a global load vector \mathbf{F}^G , respectively. After enforcing proper boundary condition for the pivot, a Cholesky decomposition technique solves for the global displacement vector \mathbf{u}^G .

3.4.2. Analytical Solution for Pad Elastic Deformations

The analytical solution for pad elastic deformations includes analysis for bending deformations in the pad and for the compression/expansion in the pad liner layer, both superpositioned to calculate the total deformation on a pad top surface. The following describes each model.

Elastic Deformation in a Pad

The present work follows the analytical model by Sternlicht et al. [8] to calculate pad axial elastic deformations, induced both thermally and mechanically. Timoshenko's plate theory [17, 18] states that the axial deformation $w_{(r,\theta)}$ of a plate subjected to a static pressure $P_{(r,\theta)}$ and temperature gradient $\Delta T_{(r,\theta)}$ across thickness is governed by,

$$\nabla^4 w = \frac{12(1 - \nu^2)P}{Et_p^3} + \frac{1 + \nu}{t_p} \nabla^2(\alpha_T \Delta T) \quad (13)$$

Eqn. (13) only accounts for bending mode deformations and disregards any axial compression/expansion. Ref. [8] suggests to use a series of (dimensionless) shape functions $f_{(r,\theta)}^i$ to represent the axial deformations on the pad top surface. Appendix B describes the selected shape functions consistent with the geometry of a point pivot (2D tilting) and a line pivot (1D tilting). Thus, the axial deformations on the pad top surface are

$$w(r, \theta) = \sum_{i=1} A_i f^i(r, \theta) \quad (14)$$

where A_i are weight coefficients. The mechanical loading energy associated with hydrodynamic pressure acting on the pad top surface is

$$W_M = \iint_S P_{(r,\theta)} w_{(r,\theta)} dS \quad (15)$$

Thermal loading is also represented by an equivalent mechanical loading including a moment on the pad borders,

$$M_r = M_\theta = \frac{Et_p^2}{12(1 - \nu)} \alpha_T \Delta T \quad (16)$$

where t_P is the pad surface and a gradient of moments on the pad top surface,

$$m_r = -(1 + \nu)\alpha_T \frac{\partial M_r}{\partial r} \quad (17a)$$

$$m_\theta = -(1 + \nu)\alpha_T \frac{\partial M_\theta}{r \partial \theta} \quad (17b)$$

Thus, the thermal loading is,

$$W_T = \iint_S \left(-m_r \frac{\partial w}{\partial r} - m_\theta \frac{\partial w}{r \partial \theta} \right) dS - \int_\Gamma M_l \frac{\partial w}{\partial \bar{\mathbf{n}}} d\Gamma \quad (18)$$

where Γ represents the boundary around the pad top surface with $\bar{\mathbf{n}}$ as a normal vector. Appendix B includes equations to calculate the bending energy V_B , hence, all terms of energy V_B , W_P , and W_T are functions of axial deformations in a pad top surface and, in case of using shape functions, are in fact linear functions of coefficients A_i . Thereafter, the principle of minimum energy helps to solve for shape function coefficients A_i .

Deformation of Pad Liner

Ref. [19] states that the total deformation of a liner layer ($w_{L(r,\theta)}$) is the superposition of a compression mode due to static pressure $P_{(r,\theta)}$ and an expansion mode induced by the temperature rise $\Delta T_{L(r,\theta)}$,

$$w_{r,\theta}^L = t_L \left(\frac{(1 + \nu_L)(1 - 2\nu_L)}{E_L(1 - \nu_L)} P - \alpha_{T_L} \Delta T \right) \quad (19)$$

with t_L as the liner thickness, ν_L and E_L as its Poisson ratio and elasticity module, and α_{T_L} is the liner thermal expansion coefficient.

3.4.3. Substructuring Analysis for Pad Mechanical Deformations (Reduction of DOFs)

As Section 3.4.1 describes, A structural FE model for a pad predicts 3D displacement fields for the entire pad volume. Assuming a rigid pivot, the displacement vector \mathbf{u}^G induced by an applied load \mathbf{F}^G is

$$\mathbf{K}^G \mathbf{u}^G = \mathbf{F}^G \quad (20)$$

where \mathbf{K}^G is a global stiffness matrix with a dimension of $3n \times 3n$ and n is the number of nodes. However, the axial DOFs of nodes attached to the pad top surface are the only

DOFs subjected to mechanical (the hydrodynamic pressure) loading. These are called active DOFs. Additionally, for a deformed pad, active DOFs are the only DOFs influencing the fluid film geometry and consequently the performance of the thrust bearing. Hence, reorganizing Eqn. (22) in terms of active and inactive DOFs, i. e.,

$$\begin{bmatrix} \mathbf{K}_{11} & \mathbf{K}_{01} \\ \mathbf{K}_{01} & \mathbf{K}_{00} \end{bmatrix} \begin{Bmatrix} \mathbf{u}_1 \\ \mathbf{u}_0 \end{Bmatrix} = \begin{Bmatrix} \mathbf{F}_p \\ 0 \end{Bmatrix} \quad (21)$$

After some manipulations, Eqn. (21) becomes,

$$\left(\mathbf{K}_{11} - \mathbf{K}_{01} \mathbf{K}_{00}^{-1} \mathbf{K}_{01} \right) \mathbf{u}_1 = \mathbf{K}_R \mathbf{u}_1 = \mathbf{F}_p \quad (22)$$

where \mathbf{K}_R is a reduced global stiffness matrix. Compared to a full global stiffness matrix \mathbf{K}^G , the reduced stiffness matrix \mathbf{K}_R is substantially smaller, hence, simpler to store and faster to process.

4. VALIDATION OF THE ANALYTICAL SOLUTION AND FE MODEL FOR PAD DEFORMATIONS

This section compares predictions from the current model for pad elastic deformations against those delivered by a commercial Finite Element software package, i.e. ANSYS[®] Mechanical APDL. As prior sections detail, elastic deformations of a pad top surface in the axial direction are modeled through two methods: a FE model and an analytical solution. Hence, predictions delivered by these methods are compared to an ANSYS[®] computational analysis for two types of TPTBs. The first type is a 60% offset cylindrical pivot (1D tilting) TPTB and the second type is a 50% offset spherical pivot (2D tilting) TPTB.

4.1. VALIDATIONS OF PAD AXIAL DEFORMATIONS FOR A CYLINDRICAL PIVOT TPTB

This report uses the configuration of a cylindrical pivot TPTB tested by Guo et al.[20] to compare predictions for pad top surface axial elastic deformations. Table 2 lists the geometry, lubricant properties, operating conditions, and thermal properties of the TPTB, Figure 5 shows a schematic view of the pad. The bearing has 3 pads, each 220 mm in OD, 110 mm in ID, 45° in arc length, and supported on 60% offset cylindrical pivots. The bearing operates at 3 krpm rotor speed ($\Omega R_o = 35$ m/s) and under a 1 MPa specific load per pad. The bearing is assumed to operate with no thrust collar misalignment.

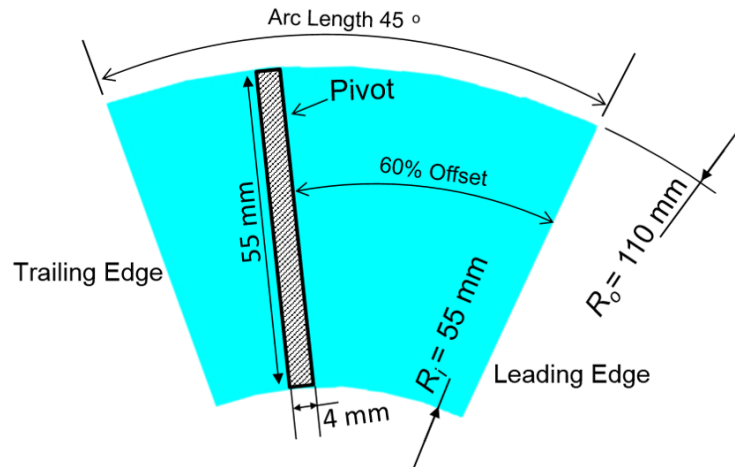


Figure 5: A schematic view of a cylindrical pivot pad in Guo et al.[20]. (Not to scale)

Table 2: Characteristics of a cylindrical pivot in Guo et al. [20]

| Bearing properties | | |
|--|---------------------|-------------------|
| Number of pads, N_P | 3 | |
| Inner diameter | 110 | mm |
| Outer diameter | 220 | mm |
| Pad arc length | 45 | ° |
| Pivot circumferential offset | 60 | % |
| Pad thickness | 27 | mm |
| Pivot Length | 55 | mm |
| Pivot width | 4 | mm |
| Pad area, A_P | 35.6 | cm ² |
| Operating condition | | |
| Specific Load $W/(N_P A_P)$ | 1.0 | cm ² |
| Shaft rotational speed | 3 | krpm |
| Max surface speed ΩR_o | 23 | m/s |
| Lubricant supply pressure | 0 | bar |
| Fluid properties | | ISO VG32 |
| Viscosity at supply temperature | 54 | cPoise |
| Viscosity temperature coefficient* | 0.0247 | 1/°C |
| Density | 821 | kg/m ³ |
| Specific heat capacity | 2.17 | kJ/(kg·K) |
| Thermal conductivity | 0.13 | W/(m·K) |
| Pad material properties* | | Steel |
| Thermal conductivity | 51 | W/(m·K) |
| Elasticity modulus | 210 | GPa |
| Thermal expansion | 12×10^{-6} | 1/°C |
| Poisson ratio | 0.3 | - |
| Thermal properties* | | |
| Reference temperature (for elastic analysis) | 20 | °C |
| Thermal mixing coefficient λ | 0.8 | - |

* Assumed or calculated based on the available data.

Figure 6 (a) shows an ANSYS[®] 3D model of a pad with boundary conditions applied at the pivot location. The nodes at the pivot are set to a zero axial displacement constraint. Figure 6 (b) and (c) depict predictions for the hydrodynamic pressure field and temperature field for the operating conditions listed in Table 2. The peak pressure is 2.4 MPa. The pad maximum temperature is 61°C located near the trailing edge and outer radius corner. Figure 6 (d) demonstrates ANSYS[®] predictions for the pad axial deformations due to pressure and thermal loading.

In Figure 6 (d), observe that ANSYS[®] predictions include the axial displacement for the pad in both the forward (positive) and backward (negative) directions. A forward

displacement indicates that a point has moved closer to the thrust collar and leads to a reduction in the film thickness. The bending and compression of a pad only contribute to a backward displacement (away from thrust collar). Nonetheless, local expansions in the axial direction may produce a forward displacement. The maximum forward displacement is $9 \mu\text{m}$ for a point near the trailing edge at the pad top surface (pad peak temperature spot). But, the maximum backward displacement is $23 \mu\text{m}$ at the leading edge of the pad back surface. Note that only the displacements on the pad top surface change the fluid film geometry and influence the bearing performance.

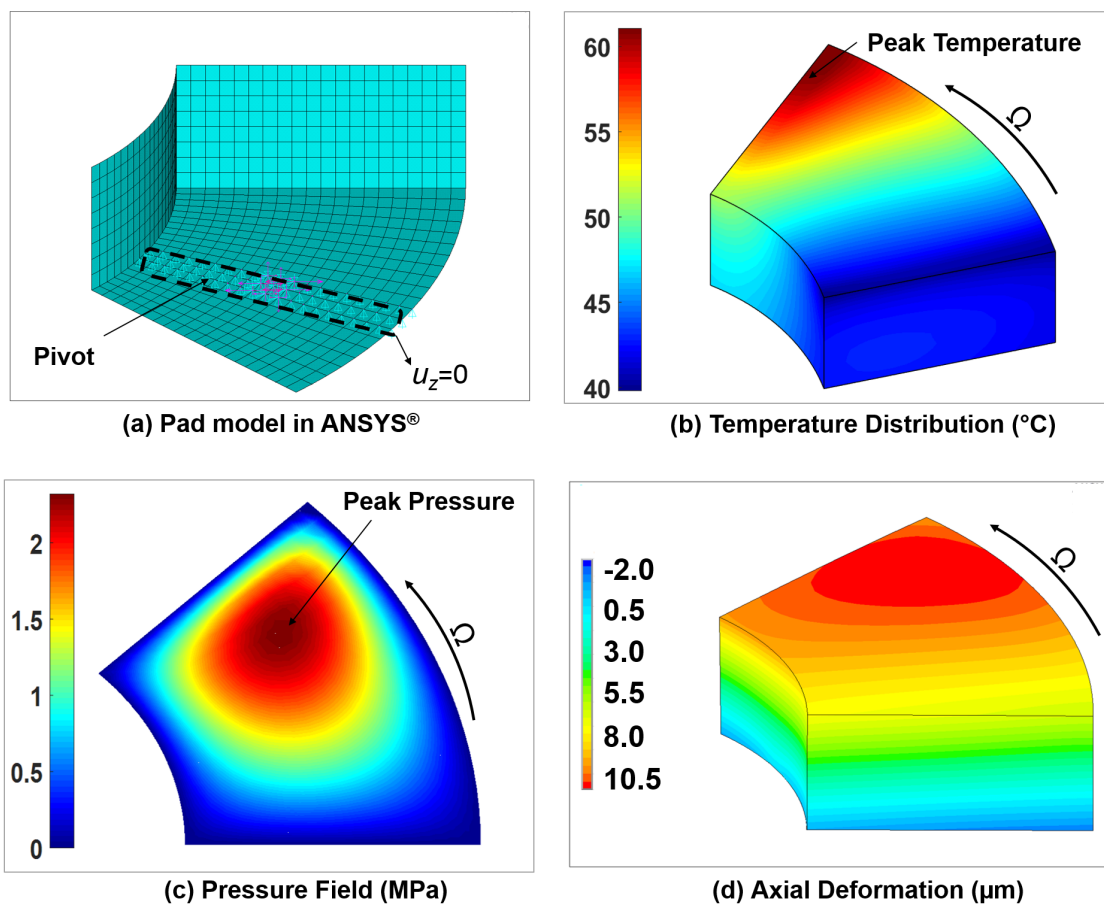


Figure 6: : (a) Pad model and boundary conditions at pivot in ANSYS®, (b) temperature distribution in pad, (c) hydrodynamic pressure field acting on pad, and (d) contour of pad axial deformations (μm). Results for cylindrical pivot pad taken from Ref.[20], rotor speed = 3 krpm, applied specific load = 1 MPa, supply temperature = 20°C. Cylindrical pivot taken from Ref.[20]

Figure 7 shows predictions for the pad top surface deformations from ANSYS® ver-

sus those obtained by the current model using the analytical solution and the in-house FE model. Deformations are due to the combined actions of pressure and temperature in a pad. Pad top surface axial deformations obtained by the FE model almost exactly match with those delivered by ANSYS[®]. The maximum difference between ANSYS[®] predictions and analytical solution is 15%. The main reason is that the analytical solution only accounts for the bending mode of deformations and disregards local axial expansion/compression. Thus, elastic deformations are a direct function of the distance from the pivot line.

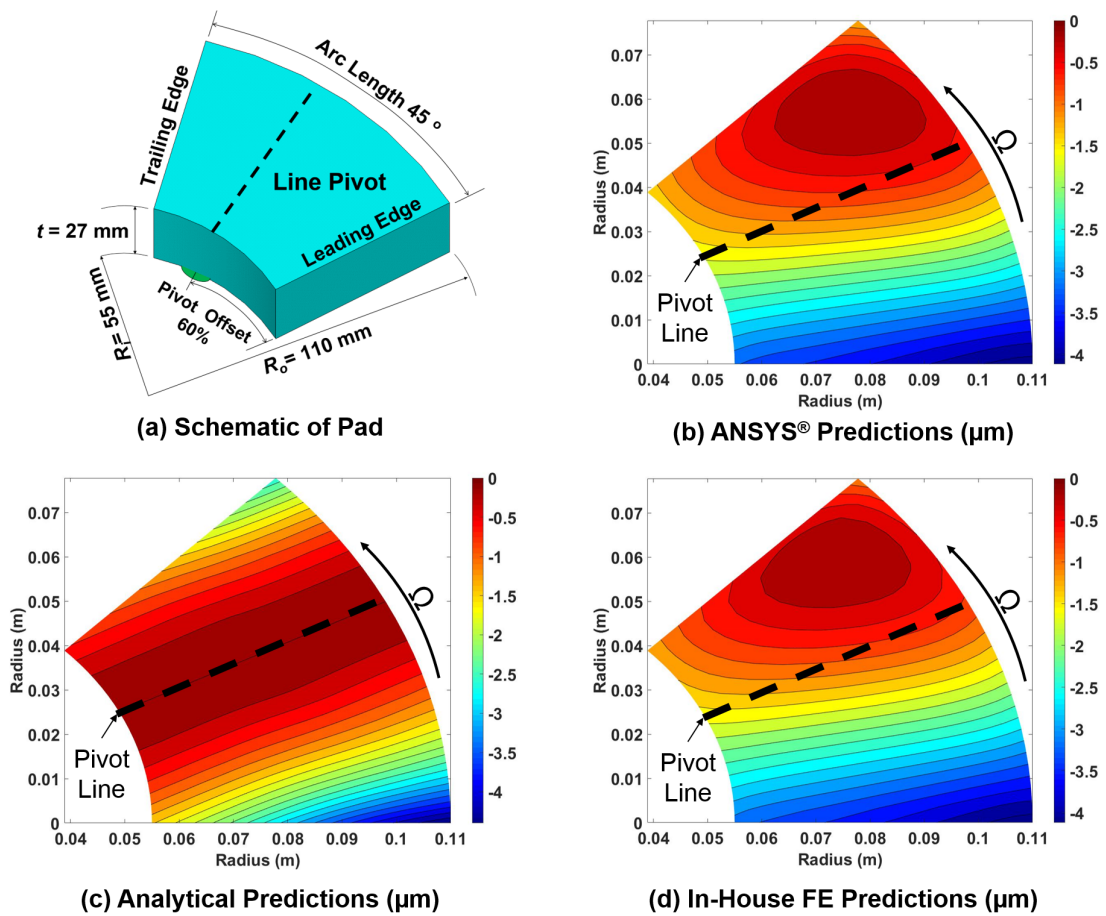


Figure 7: Axial deformations (μm) on top surface of pad due to combined action of pressure and temperature as obtained by (b) ANSYS[®], (c) an analytical solution, (d) an in-house FE model. Results for cylindrical pivot pad in Ref.[20], rotor speed = 3 krpm, applied specific load = 1 MPa, supply temperature = 20 °C.

4.2. VALIDATIONS OF PAD AXIAL DEFORMATIONS FOR A SPHERICAL PIVOT TPTB

The configuration of a spherical pivot TPTB tested by Mikula [21] is used to evaluate predictions of pad axial deformations. Table 2 outlines the geometry, lubricant properties, operating conditions, and thermal properties of the TPTB. Figure 8 shows a schematic view of the pad. The bearing has 8 pads, each 267 mm in OD and 133 mm in ID, 39° in arc length, and supported on 50% offset spherical pivots. The bearing operates at 3 krpm ($\Omega R_o = 41$ m/s) and under a 1 MPa specific load per pad. The bearing is assumed to work with a aligned thrust bearing.

Table 3: Characteristics of a point pivoted TPTB tested by Mikula. [21]

| Bearing properties | | |
|---|---------------------|-------------------|
| Number of pads, N_P | 8 | |
| Inner diameter | 133 | mm |
| Outer diameter | 267 | mm |
| Pad arc length | 38 | ° |
| Pivot circumferential offset | 50 | % |
| Pivot radial offset | 50 | % |
| Pad thickness* | 23 | mm |
| Pivot radius* | 15 | mm |
| Pad area, A_P | 45.6 | cm ² |
| Operating condition | | |
| Specific Load $W/(N_P A_P)$ | 1.0 | MPa |
| Shaft rotational speed | 3 | krpm |
| Max surface speed ΩR_m | 41 | m/s |
| Lubricant supply pressure | 0 | bar |
| Fluid properties | | ISO VG32 |
| Viscosity at supply temperature* | 22 | cPoise |
| Viscosity temperature coefficient* | 0.0247 | 1/°C |
| Density | 821 | kg/m ³ |
| Specific heat capacity | 2.17 | kJ/(kg·K) |
| Thermal conductivity | 0.13 | W/(m·K) |
| Pad material properties | | Steel |
| Thermal conductivity | 51 | W/(m·K) |
| Elasticity modulus | 210 | GPa |
| Thermal expansion | 12×10^{-6} | 1/°C |
| Poisson ratio | 0.3 | - |
| Thermal properties* | | |
| FE reference temperature (for elastic analysis) | 20 | °C |
| Thermal mixing coefficient λ | 0.8 | - |

*Assumed or calculated based on the available data.

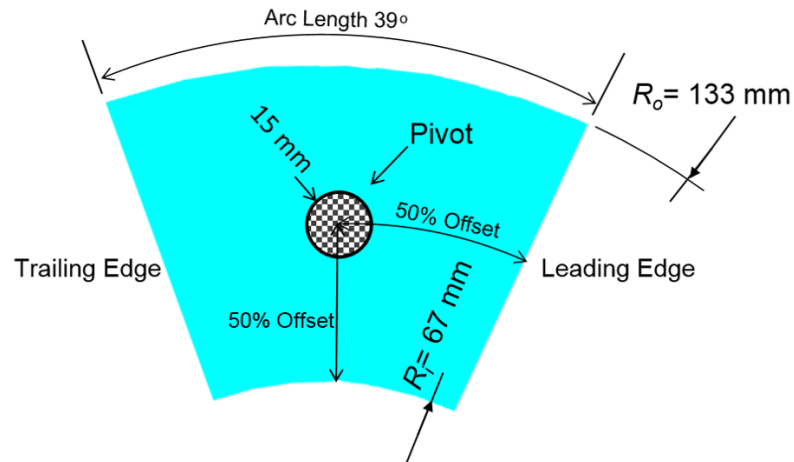


Figure 8: A schematic view of a spherical pivot pad in Mikula [20]. (Not to scale)

Figure 9 (a) depicts the spherical pivot pad modeled in ANSYS[®] with boundary conditions applied on the pivot. All nodes on the pivot-pad surface are constrained to zero axial displacement. Figure 9 (b) and (c) show predictions for the hydrodynamic pressure field and pad temperature field for the operating conditions listed in Table 3. The pad maximum temperature is 106°C and the peak pressure is 2.1 MPa. Note that the peak pressure is located on top of the pivot at the pad center point.

Figure 9 (d) shows ANSYS[®] predictions for pad elastic deformations in the axial direction, induced by the combined action of pressure and temperature. The pad maximum displacement in the forward direction is 20.4 μm for a point on the pad top surface and in the retract direction is 5.5 μm at the leading edge of the pad back surface. Note that the pad peak forward displacement occurs at the peak temperature point. In general, deformations of the pad top surface add 11 μm into the variations of the fluid film thickness.

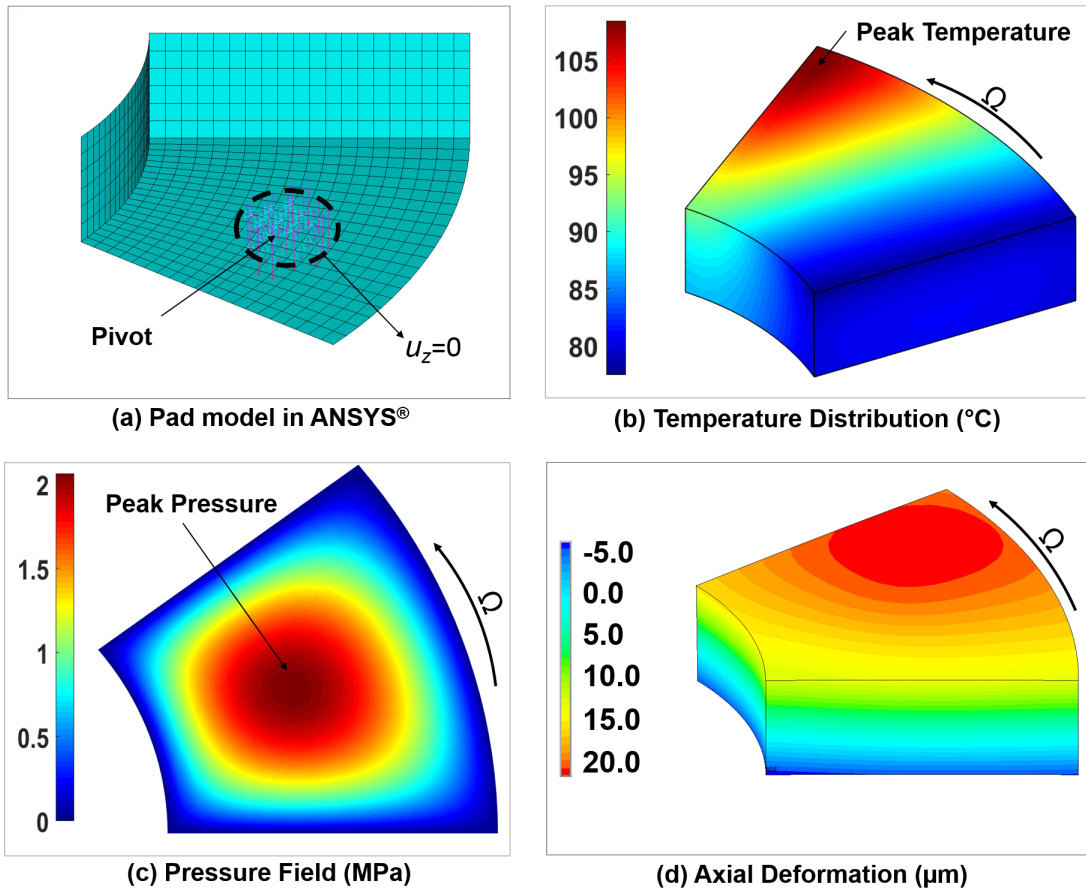


Figure 9: : (a) Pad model and boundary conditions at pivot in ANSYS®, (b) temperature distribution in pad, (c) hydrodynamic pressure field acting on pad, and (d) contour of pad axial deformations (μm). Results for cylindrical pivot pad taken from Ref.[20], rotor speed = 3 krpm, applied specific load = 1 MPa, supply temperature = 46 °C.

Figure 10 shows predictions for the pad top surface axial deformations obtained through ANSYS® versus those calculated by the analytical solution and the FE model. FE predictions are in a very good agreement with ANSYS® analysis with a maximum difference of 1.2%. Predictions of the analytical solution show a maximum of 40% difference with ANSYS® analysis.

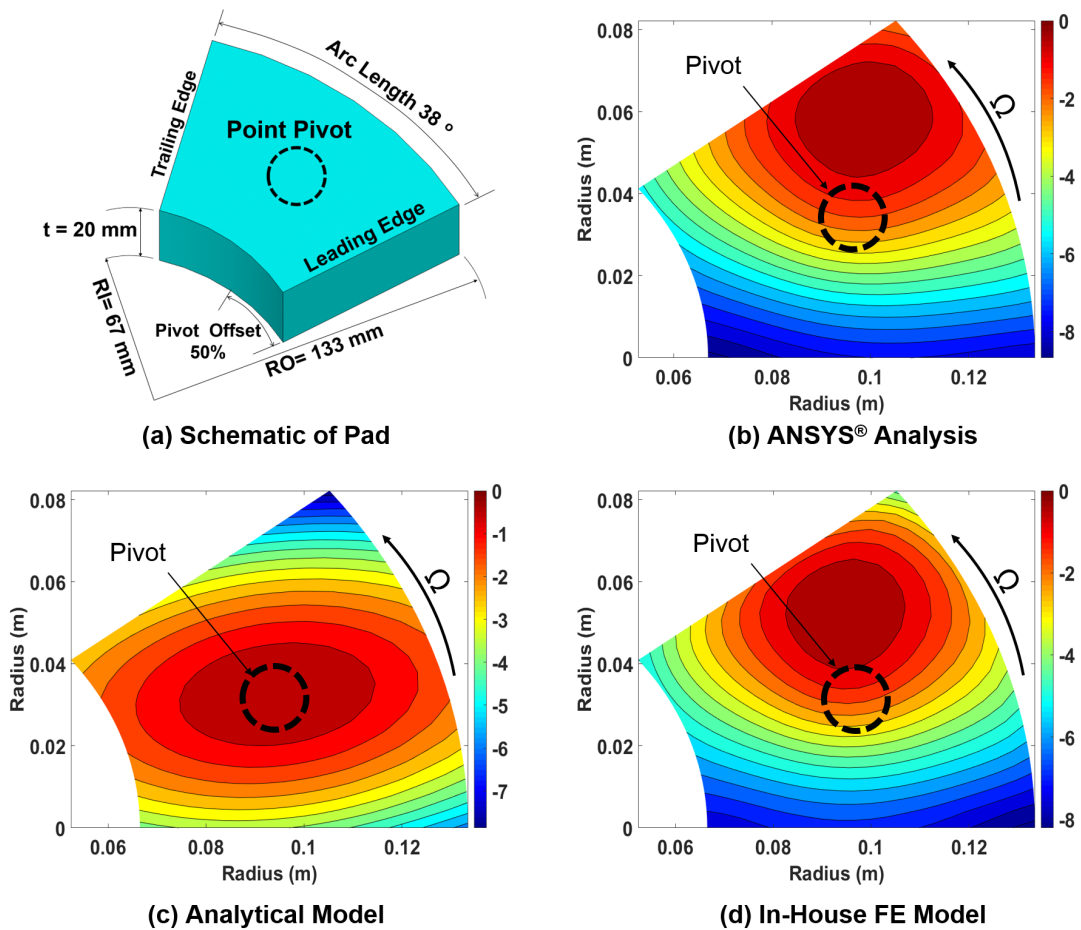


Figure 10: Axial deformations (μm) on top surface of pad due to combined action of pressure and temperature as obtained by (b) ANSYS®, (c) an analytical solution, (d) a FE model. Results for spherical pivot pad in Ref.[20], rotor speed = 3 krpm, applied specific load = 1 MPa, supply temperature = 46 °C.

5. COMPARISON OF PREDICTIONS VERSUS TEST DATA

Mikula [21] also measured pad (subsurface) temperatures in a double-sided tilting pad thrust bearing operating under both laminar and turbulent flow conditions. A double-sided TPTB has two bearings installed on the opposite sides of a thrust collar, one acts against a primary axial load in the system (active side) while the other one reacts to occasional reverse-direction momentary loads (inactive or slack-side). Figure 11 shows a schematic view of the test rig with a gas turbine driving the main shaft of the rig through a flexible coupling with a controlled speed from 4 to 13 krpm. The main shaft/collar is positioned with a fixed bearing housing on one side and an axially sliding bearing housing on the other side. A hydraulic system applies load on the sliding housing and moves it toward the fixed one. Hence, test TPTB ① is forced against collar ① and collar ② is pushed against slave TPTB ②. This arrangement creates an identical loading on the test bearings ① and ②. Oil control rings, shrouded on the thrust collar, divert the discharge oil and reduce the hot oil carry over. Teflon oil seal rings also act to prevent oil leakage out of the bearing housings or into the journal bearings. A flooded lubrication system is used to supply cold oil into the test bearings.

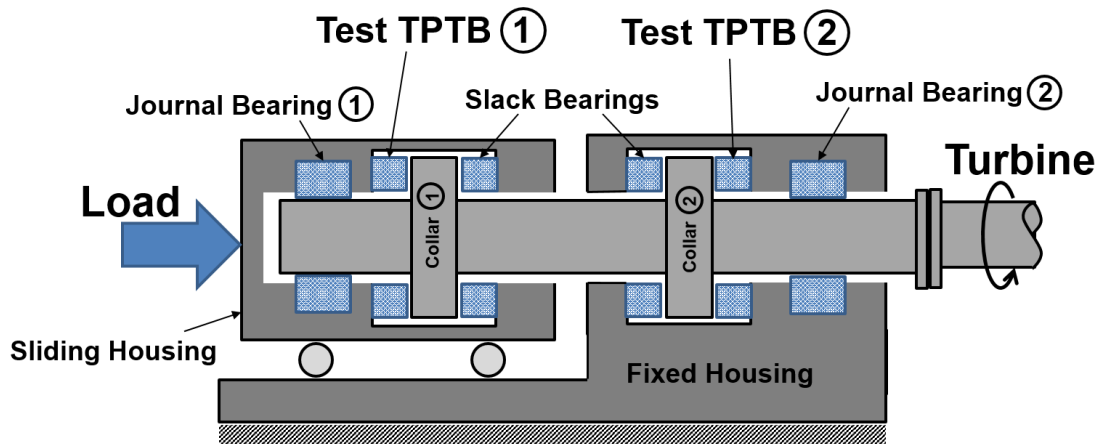


Figure 11: Schematic view of a test rig in Mikula [21] to evaluate the operating characteristics of laminar and turbulent flow TPTBs.

Table 4 outlines the geometry, lubricant properties, and operating conditions of the eight-pad bearing 267 mm in OD and 133 mm in ID, each pad is supported on 50% offset (centrally pivoted) rocker back (2D tilting) pivots. A pad top surface is covered with a 2

mm thick Babbitt layer, and thermocouples are positioned within 0.8 mm depth from the Babbitt surface. The rotor speed ranges from 4 to 13 krpm and gives a outer surface speed between $\Omega R_o = 54$ to 181 m/s. The load applied (W_z) on the bearing is between 200 kN to 1 MN, equivalent to a specific load per pad ($\frac{W_z}{A_P N_P}$) ranging from 0.69 to 3.44 MPa. The bearing is assumed to operate under no thrust collar misalignment.

Table 4: Characteristics of a point-pivot TPTB tested by Mikula. [21]

| Bearing properties | | | |
|---|---------------------|---------------------|---------|
| Number of pads, N_P | 8 | | |
| Inner diameter | 133 | mm | |
| Outer diameter | 267 | mm | |
| Pad arc length | 39 | ° | |
| Pivot circum. offset | 50 | % | |
| Pivot radial offset | 50 | % | |
| Pad thickness* | 25 | mm | |
| Babbitt thickness* | 2 | mm | |
| Pivot radius* | 15 | mm | |
| Pad area A_P | 45.6 | cm ² | |
| Operating conditions | | | |
| Specific load $W_z/(A_P N_P)$ | 0.69-3.44 | MPa | |
| Shaft rotational speed | 4-13 | krpm | |
| Mean surface speed ΩR_m | 41-136 | m/s | |
| Lubricant supply pressure | 1.0 | bar | |
| Fluid properties | | | |
| | ISO VG32 | | |
| Viscosity at supply temperature | 22 | mPa·s | |
| Viscosity temperature coefficient | 0.0247 | 1/°C | |
| Density | 821 | kg/m ³ | |
| Specific heat capacity | 2.17 | kJ/(kg·K) | |
| Thermal conductivity | 0.13 | W/(m·K) | |
| Pad material properties | | | |
| | Steel | Babbitt | |
| Thermal conductivity | 51 | 24 | W/(m·K) |
| Elasticity module | 210 | 52 | GPa |
| Thermal expansion | 12×10^{-6} | 26×10^{-6} | 1/°C |
| Poisson ratio | 0.3 | 0.3 | - |
| Thermal properties* | | | |
| Reference temperature (for elasticity analysis) | 20 | | °C |
| Thermal mixing coefficient λ | 0.4-0.6 | | - |

*Assumed or calculated based on the available data.

The TPTB operates at speeds that determine either laminar flow, transition from laminar to turbulent flow, or turbulent flow as based on a characteristic circumferential Reynolds number, $Re = \frac{R_m \Omega \rho h_{min}}{\mu}$ where R_m is the mean radius, h_{min} is the minimum fluid film thick-

ness, Ω is the rotor speed, and ρ and μ are the fluid density and viscosity averaged across the film thickness. The flow remains laminar with a Reynolds number $Re < 580$ (Re_L : lower critical Reynolds number), and transits to fully turbulent at $Re > 800$ (Re_U : upper critical Reynolds number) [22, 23].

The following shows a comparison of the measurements in Ref.[21] against predictions based on a TEHD analysis that includes pressure and temperature induced pad elastic deformations. TEHD predictions based on the analytical solution and the in-house FE model for elastic deformations (described earlier) are shown. Figure 12 depicts the pad schematic view with thermocouple locations.

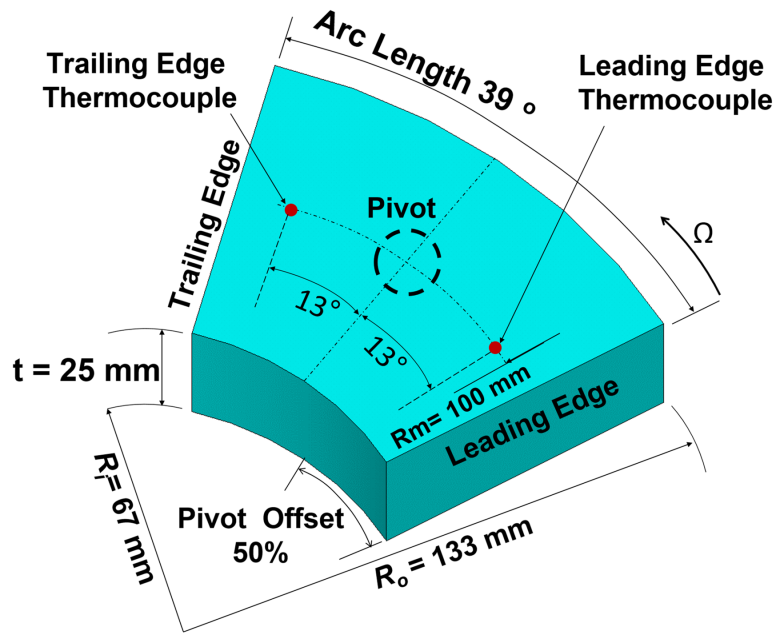


Figure 12: Schematic view of pad and location of thermocouples placed under top surface. Details taken from [21]

Operation under Laminar Flow Condition

Figure 13 shows a circumferential Reynolds number at the minim film thickness for the test TPTB operating at 4 krpm ($R_o\Omega=54$ m/s) and under applied load ranging between 0.69 to 3.44 MPa. The maximum Reynolds number associated with the slightest load (0.69 MPa) is 424 and decreases down to 199 under the largest applied load (3.44 MPa). Hence, the operating remains below the lower band of critical Reynolds number ($Re_L=580$) and the flow is laminar.

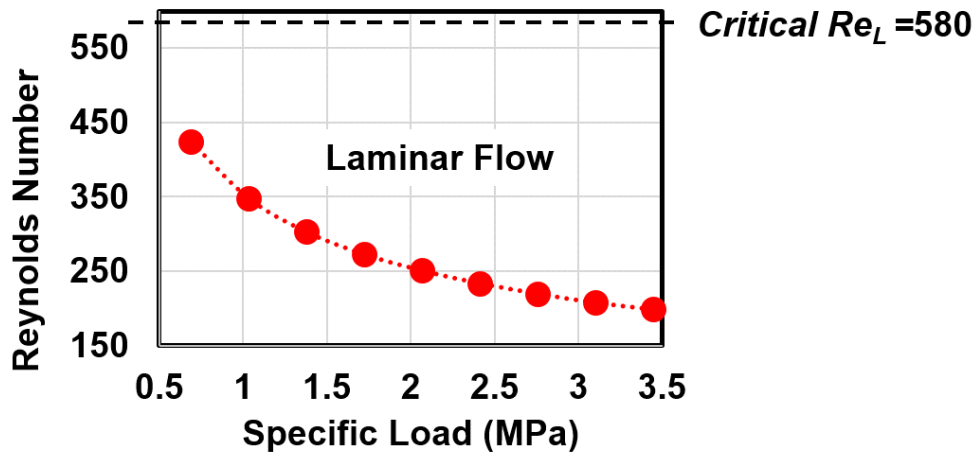


Figure 13: Circumferential Reynolds number at minimum film thickness. (Supply temperature = 46°C, rotor speed = 4 krpm, laminar flow condition)

Figure 14 depicts the measured pad subsurface temperature rise and current model predictions versus specific load (a) at the pad leading edge and (b) at the pad trailing edge. For low to moderate specific loads (<2 MPa), predictions with analytical solutions for pad elastic deformations align closely with those obtained with the FE model but slightly differ as the applied load increases. In general, predictions using the FE model best match with test data with a maximum difference of 3°C. Predictions using the analytical solution match test data with a maximum difference of 8°C.

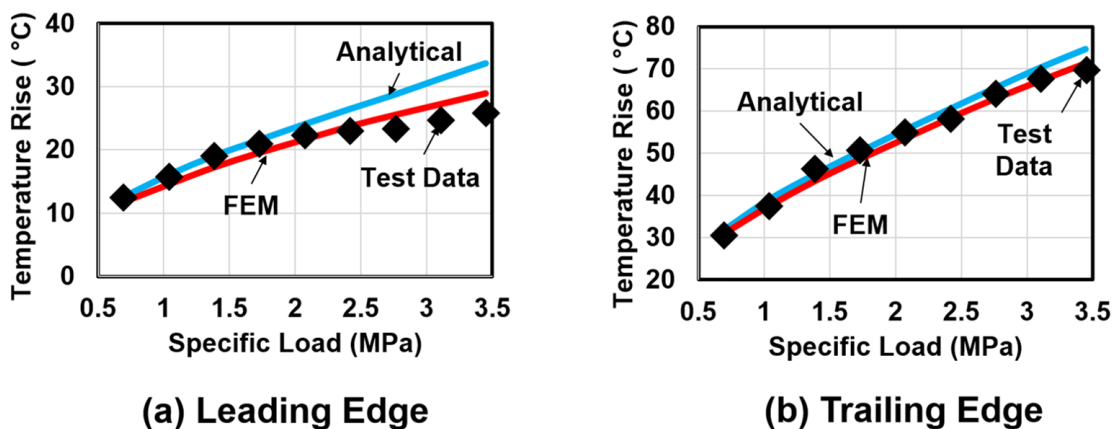


Figure 14: Pad subsurface temperature rise versus specific load at pad (a) leading edge and (b) trailing edge. Test data from Ref.[21] versus predictions from the current TEHD model: analytical solution and an in-house FE method. (Supply temperature = 46°C, rotor speed = 4 krpm, laminar flow condition)

Operation under Turbulent Flow Condition

Figure 15 demonstrates the predicted characteristic circumferential Reynolds number for the test TPTB operating at 10 krpm of rotor speed ($R_o\Omega=135$ m/s) and specific load ranging from 0.69 to 3.44 MPa. The Reynolds number is at its maximum of 1675 at the slightest load (0.69 MPa) and goes to its minimum of 787 at the largest load. The upper band of critical Reynolds number is $Re_U=800$. Accordingly, the flow is turbulent for specific loads below 2.75 MPa and turns into the transition zone under a larger load. A transition from turbulent to laminar is followed by a fast increase in the temperature as the thermal mixing in the flow lessens.

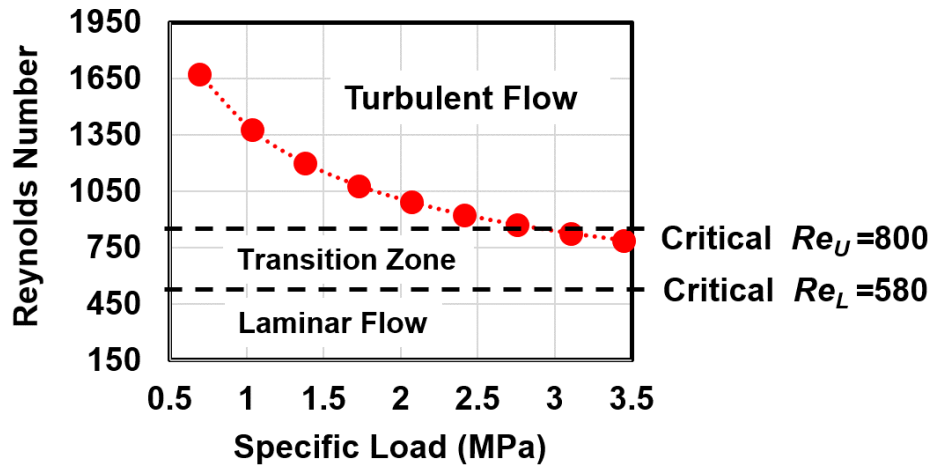


Figure 15: Circumferential Reynolds number at the minimum film thickness. (Supply temperature = 46°C, rotor speed = 10 krpm, turbulent flow condition)

Figure 16 benchmarks test data from Ref.[21] for pad subsurface temperature rise against predictions obtained from the current model for (a) the pad leading edge and (b) the pad trailing edge. Predictions with the FE model for pad show a good agreement with test data. Predictions for pad subsurface temperature using the analytical solution show a larger difference with test data than that in FE predictions. The maximum difference with test data is 19% for FE predictions and 45% for analytical predictions.

Figure 17 depicts the test data for pad subsurface temperature rise versus predictions using a turbulent flow model and a laminar flow model. TEHD predictions are based on the in-house FE model. Laminar flow predictions disagree with test data with a maximum difference of 17°C (50%) at the leading edge and 33°C (50%) at the trailing edge. Turbulent flow predictions, however, are substantially better with a maximum difference of

10°C (20%) from test data.

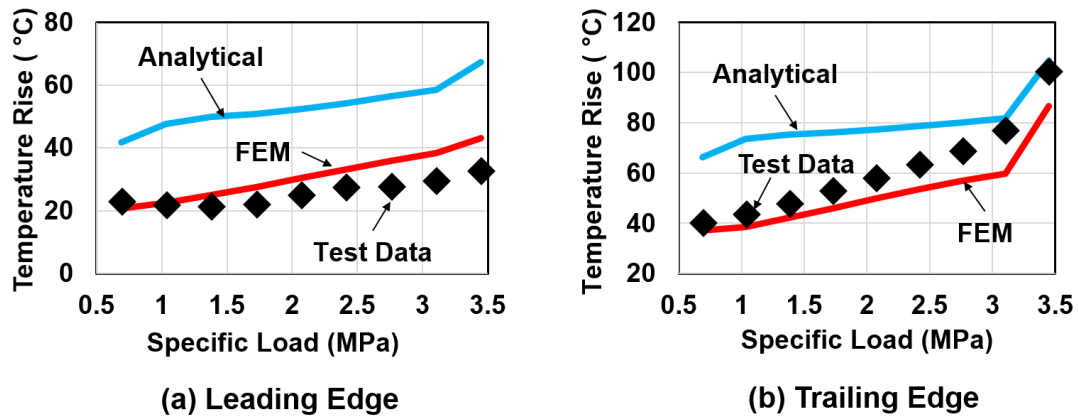


Figure 16: TEHD predictions versus measurements for pad subsurface temperature rise versus specific load at pad (a) leading edge and (b) trailing edge using an analytical solution and a FE model. Test data from Ref.[21]. (Supply temperature = 46°C, rotor speed = 10 krpm, turbulent flow condition)

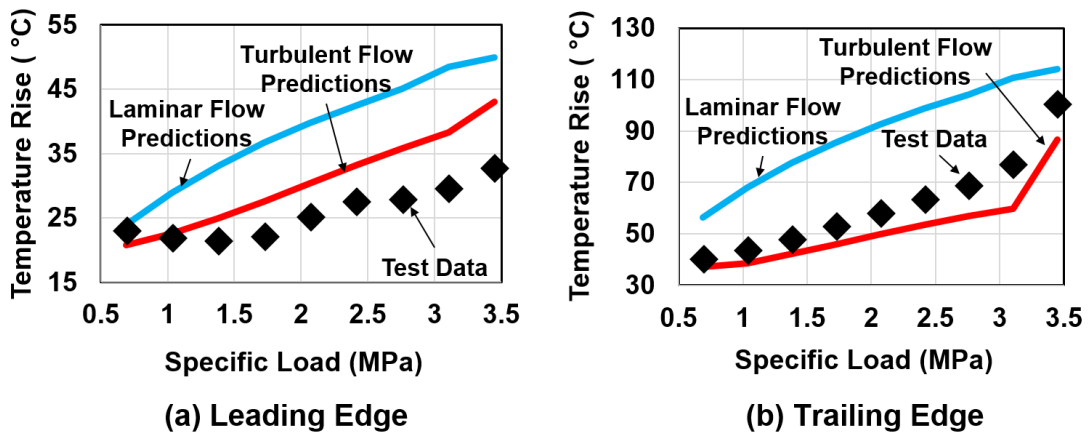


Figure 17: Laminar flow and turbulent flow predictions versus measurements for pad subsurface temperature rise at pad (a) leading edge and (b) trailing edge. Test data from Ref.[21]. (Supply temperature = 46°C, rotor speed = 10 krpm, turbulent flow condition)

Operation in Transition Zone from Laminar Flow to Turbulent Flow

Figure 18 shows the characteristic circumferential Reynolds number for the test TPTB under 3.44 MPa specific load with a rotor speed ranging from 4 to 13 krpm ($R_o\Omega=54-181$ m/s). The Reynolds number is 199 at the lowest rotor speed (4 krpm) and the flow is laminar. With the rotor speed at 9 krpm, the Reynolds number rises to 672 and the

flow moves into transition zone (larger the lower critical band $Re_L=580$). A transition from laminar to turbulent is followed by a fast drop in the temperature due to the enhance thermal mixing in the flow. For rotor speeds above 11 krpm, the Reynolds number is larger than the upper critical band ($Re_U=800$) and the flow is fully turbulent.

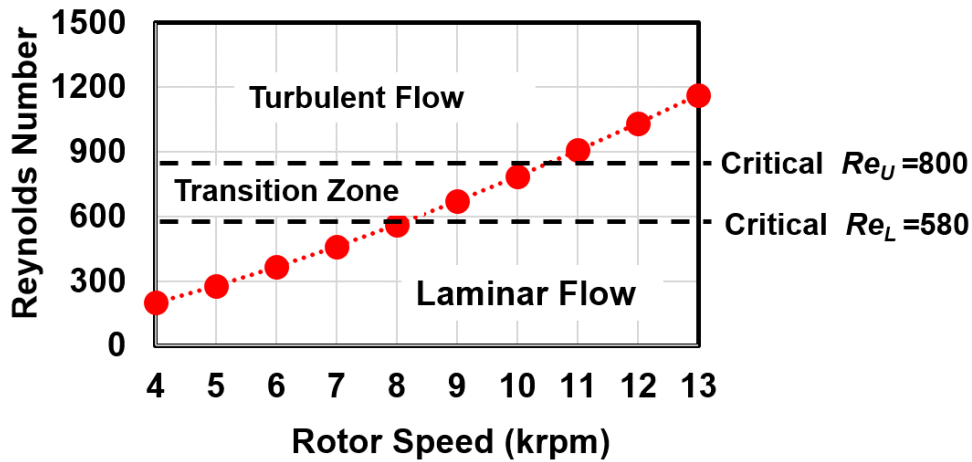
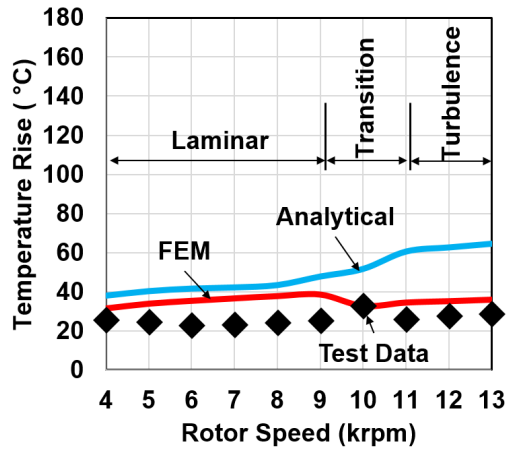


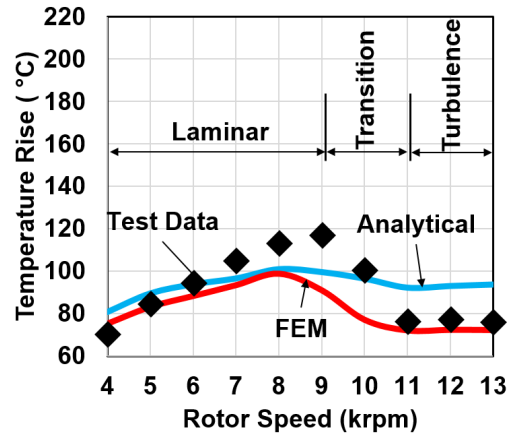
Figure 18: Circumferential Reynolds number at the minimum film thickness. (Supply temperature = 46°C , specific load = 3.44 MPa)

Figure 19 shows predictions along with test data for pad subsurface temperature rise at (a) the pad leading edge and (b) the pad trailing edge versus rotor speed. TEHD predictions show a good agreement with test data. Predictions based on the FE model of pad elastic deformations demonstrates a better match with test data with a maximum difference of 25%.

Figure 20 compares the test data to predictions for the pad subsurface temperature rise at (a) the pad leading edge and (b) the pad trailing edge versus rotor speed. Predictions are from the current model using the the laminar flow and the turbulent flow analyses. Observe that the turbulent flow predictions follow the trend of the test data with a substantially lesser difference than that in laminar predictions. At rotor speeds above 9 krpm, the flow begins to transits to turbulent, hence, the thermal mixing increases in the film and temperature notably drops. As the pad operates with a fully turbulent flow (>11 krpm), the temperature again increases with rotor speed but with a much lesser rate than that in a laminar flow.

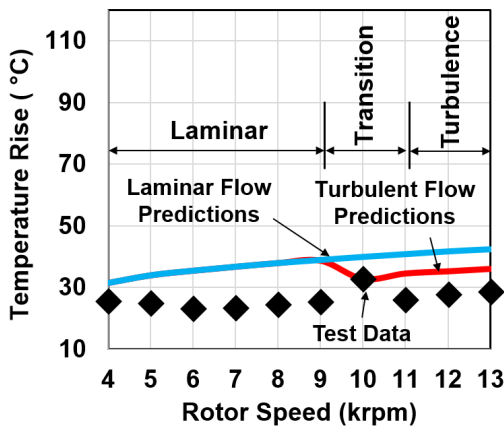


(a) Leading Edge

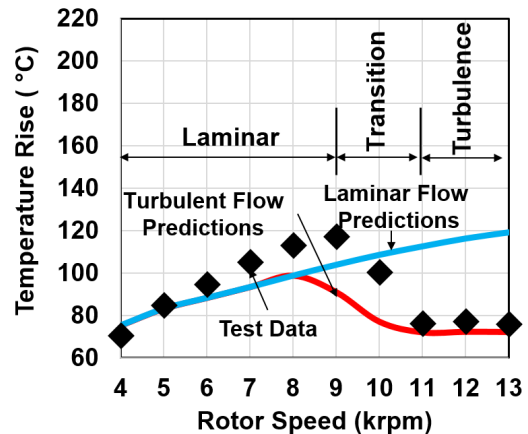


(b) Trailing Edge

Figure 19: TEHD predictions and measured pad subsurface temperature rise versus rotor speed at pad (a) leading edge and (b) trailing edge. Test data from Ref.[21]. (Supply temperature = 46 °C , specific load = 3.44 MPa)



(a) Leading Edge



(b) Trailing Edge

Figure 20: Turbulent flow and laminar flow predictions versus measurements for pad subsurface temperature rise for pad (a) leading edge and (b) trailing edge. Test data from Ref.[21]. (Supply temperature = 46 °C, specific load = 3.44 MPa)

CLOSURE

This report describes a multiple-pad thermo-elasto-hydrodynamic (TEHD) computational analysis tool to deliver predictions for the static and dynamic force performance of tilting pad thrust bearings (TPTBs) operating under both laminar and turbulent flow conditions. The current TEHD analysis accounts for pad elastic deformations, both pressure and temperature induced, using a full 3D Finite Element model or an approximate but fast analytical solution.

A 3D thermal energy transport equation in the fluid film, coupled with heat conduction equations in the bearing elements (pads and the thrust collar), is solved collectively with a generalized Reynolds equation, allowing for cross-film viscosity variations. Then, the predicted pressure field and temperature rise are employed by a pad structure stiffness model to deliver deformations on the pad top surface, further integrated to update the fluid film geometry.

Pad subsurface temperature predictions from the current model are compared against test data for an eight-pad TPTB with 267 mm in OD operating at rotor speeds ranging from 4 to 13 krpm ($\Omega R_O = 54$ to 181 m/s) and under a specific load ($\frac{W_z}{A_P N_P}$) between 0.69 to 3.44 MPa. The operating conditions set a characteristic Reynolds number (Re at the minimum film thickness) ranging from 199 to 1675, determining a laminar flow condition for $Re < 580$ and a fully turbulent flow condition for $Re > 800$. In general, TEHD predictions using the FE model better match with test data than those from the analytical solution. In addition, accounting for turbulent flow effects improves temperature predictions up to 50% (43°C).

REFERENCES

- [1] Khonsari, M., 1987, “A Review of Thermal Effects in Hydrodynamic Bearings Part I: Slider and Thrust Bearings,” *J. Trib.*, **30**(1), pp. 19–25.
- [2] Robinson, C., and Cameron, A., 1975, “Studies in Hydrodynamic Thrust Bearings. I. Theory Considering Thermal and Elastic Distortions,” *Philosophical Transactions of the Royal Society of London A: Mathematical, Physical and Engineering Sciences*, **278**(1283), pp. 351–366.
- [3] Ettles, C., 1976, “The Development of a Generalized Computer Analysis for Sector Shaped Tilting Pad Thrust Bearings,” *J. Trib.*, **19**(2), pp. 153–163.
- [4] Almqvist, T., Glavatskikh, S., and Larsson, R., 1999, “THD Analysis of Tilting Pad Thrust Bearings-Comparison Between Theory and Experiments,” *J. Trib.*, **122**(2), pp. 412–417.
- [5] Vohr, J., 1981, “Prediction of the Operating Temperature of Thrust Bearings,” *J. Lub. Tech.*, **103**(1), pp. 97–106.
- [6] Ahmed, S., Fillon, M., and Maspeyrot, P., 2010, “Influence of Pad and Runner Mechanical Deformations on the Performance of a Hydrodynamic Fixed Geometry Thrust Bearing,” *J. Eng. Trib. Part J*, **224**(4), pp. 305–315.
- [7] San Andrés, L., and Koosha, R., 2017, Thermo Hydrodynamic (THD) Computational Analysis for Tilting Pad Thrust Bearings (TPTBs) Annual Report to TRC Meeting, Texas A&M University [Online; accessed July 2018].
- [8] Sternlicht, B., Carter, G., and Arwas, E., 1961, “Adiabatic Analysis of Elastic, Centrally Pivoted, Sector, Thrust-Bearing Pads,” *J. App. Mech.*, **28**(2), pp. 179–187.
- [9] Robinson, C., and Cameron, A., 1975, “Studies in Hydrodynamic Thrust Bearings. I. Theory Considering Thermal and Elastic Distortions,” *Philosophical Transactions of the Royal Society of London A: Mathematical, Physical and Engineering Sciences*, **278**(1283), pp. 351–366.
- [10] Brockett, t. S., Barrett, L. E., and Allaire, P. E., 1996, “Thermoelastohydrodynamic Analysis of Fixed Geometry Thrust Bearings Including Runner Deformation,” *J. Trib.*, **39**(3), pp. 555–562.
- [11] Glavatskikh, S., and Fillon, M., 2001, “TEHD Analysis of Tilting-Pad Thrust Bearings-Comparison with Experimental Data,” *Intern. Trib. Con., Japan Society of Tribologists*, pp. 1579–1584.

- [12] Robinson, C., and Cameron, A., 1975, “Studies in Hydrodynamic Thrust Bearings. II. Comparison of Calculated and Measured Performance of Tilting Pads by Means of Interferometry,” *Philosophical Transactions of the Royal Society of London A: Mathematical, Physical and Engineering Sciences*, **278**(1283), pp. 367–384.
- [13] Glavatskih, S., and Fillon, M., 2004, “TEHD Analysis of Thrust Bearings with PTFE-Faced Pads,” *ASME Intern. J. Trib. Con.*, pp. 603–613.
- [14] Radeş, M., 1972, “Dynamic Analysis of an Inertial Foundation Model,” *Intern. J. of Solids Struc.*, **8**(12), pp. 1353–1372.
- [15] Jeng, M., Zhou, G., and Szeri, A., 1986, “A Thermohydrodynamic Solution of Pivoted Thrust Pads: Part I Theory,” *J. Trib.*, **108**(2), pp. 195–207.
- [16] Brockett, t. S., 1995, “Thermoelastohydrodynamic Lubrication in Thrust Bearings,” PhD thesis, University of Virginia, Charlottesville, VA, USA.
- [17] Timoshenko, S. P., and Woinowsky-Krieger, S., 1959, *Theory of plates and shells* McGraw-hill.
- [18] Goodier, J., 1957, “Thermal stress and deformation,” *J. App. Mech.*, **24**(3), pp. 467–471.
- [19] Kuznetsov, E., Glavatskih, S., and Fillon, M., 2011, “Thd analysis of compliant journal bearings considering liner deformation,” *J. Trib. Intern.*, **44**(12), pp. 1629–1641.
- [20] Guo, A., Wang, X., Jin, J., Hua, D. Y., and Hua, Z., 2015, “Experimental test of static and dynamic characteristics of tilting-pad thrust bearings,” *Adv. Mech. Eng.*, **7**(7), pp. 1–8.
- [21] Mikula, A. M., 1986, “Evaluating tilting-pad thrust bearing operating temperatures,” *J. Trib.*, **29**(2), pp. 173–178.
- [22] Abramovitz, S., 1955, “Turbulence in a Tilting-Pad Thrust Bearing,” *J. Franklin Ins.*, **259**(1), pp. 61–64.
- [23] Gregory, R., 1974, “Performance of Thrust Bearings at High Operating Speeds,” *J. Lub. Tech.*, **96**(1), pp. 7–13.
- [24] Ng, C. W., 1964, “Fluid Dynamic Foundation of Turbulent Lubrication Theory,” *J. Trib.*, **7**(4), pp. 311–321.

A. APPENDIX: TURBULENT FLOW FUNCTIONS

In the generalized Reynolds equation, Eqn. (2), H_r, H_θ , and G are turbulent flow functions defined as, [15]

$$H_{r(\theta,t)} = \int_0^h \int_0^z \zeta_3(\bar{z}) : d\bar{z} dz - \frac{\int_0^h \zeta_3(z) dz}{\int_0^h \zeta_4(z) dz} \int_0^h \int_0^z \zeta_4(\bar{z}) d\bar{z} dz \quad (\text{A.1a})$$

$$H_{\theta(r,\theta,t)} = \int_0^h \left(\int_0^z \zeta_1(\bar{z}) d\bar{z} \right) dz - \frac{\int_0^h \zeta_1(z) dz}{\int_0^h \zeta_2(z) dz} \int_0^h \left(\int_0^z \zeta_2(\bar{z}) d\bar{z} \right) dz \quad (\text{A.1b})$$

$$G_{(r,\theta,t)} = h - \frac{1}{\int_0^h \zeta_4(z) dz} \int_0^h \left(\int_0^z \zeta_4(\bar{z}) d\bar{z} \right) dz \quad (\text{A.1c})$$

Above, ζ_i , $i = 1 : 4$ are functions of the local viscosity (μ) across the fluid film and the flow turbulence, [15]

$$\zeta_1(z) = \frac{\frac{h}{2} - z}{\mu(z)f(z)} \left(1 - \frac{g(z)}{f(z)} \right) \quad (\text{A.2a})$$

$$\zeta_2(z) = \frac{1}{\mu(z)f(z)} \left(1 - \frac{g(z)}{f(z)} \right) \quad (\text{A.2b})$$

$$\zeta_3(z) = \frac{\frac{h}{2} - z}{\mu(z)f(z)} \quad (\text{A.2c})$$

$$\zeta_4(z) = \frac{1}{\mu(z)f(z)} \quad (\text{A.2d})$$

where f and g are the turbulent flow functions obtained based on Ng and Pan [15] modeling of the flow turbulence phenomena,

$$f(z) = 1 + \frac{\epsilon_m}{\nu} = 1 + \kappa_f \left[z_c^+ - \delta_l^+ \tanh \left(\frac{z_c^+}{\delta_l^+} \right) \right] \quad (\text{A.3a})$$

$$g(z) = \tau_c \frac{\partial \left(\frac{\epsilon_m}{\nu} \right)}{\partial \tau} \Bigg|_{\tau=\tau_c} = \frac{1}{2} \kappa_f z_c^+ \tanh^2 \left(\frac{z_c^+}{\delta_l^+} \right) \quad (\text{A.3b})$$

here κ_f and δ_l^+ are Reichardt's formula coefficients and

$$z_c^+ = \frac{z}{\nu} \sqrt{\frac{\tau_c}{\rho}} \quad (\text{A.4})$$

where τ_c is the Couette shear stress,

$$\tau_c = \frac{r\Omega}{\int_0^h \frac{dz}{\mu(z)f(z)}} \quad (\text{A.5})$$

hence, an accurate assessment of f and g functions requires an iterative solution between f and,

$$\frac{\epsilon_m}{\nu} = f - 1 + \frac{\zeta_4(h)}{r\Omega} \frac{\partial P}{\partial \theta} g \left(z - \frac{h}{2} + \frac{\zeta_1(h)}{\zeta_2(h)} \right) \quad (\text{A.6})$$

Using Ng's model [24], turbulent flow effects continuously increase with Reynolds number ($Re = \frac{R\Omega\rho h}{\mu}$ where R is the radial length, h is the fluid film thickness, Ω is the rotor speed, and ρ and μ are the fluid density and viscosity averaged cross the film thickness). However, in 1955, Abramovitz [22] experimentally observes that a TPTB operating with a Reynolds number (at the minim film thickness) lower than 580 remains laminar (Re_L : lower critical Reynolds number) and transits to fully turbulent with a Reynolds number higher than 800 (Re_U : upper critical Reynolds number). Abramovitz uses mean values of fluid viscosity and film thickness for the calculation of Reynolds number. In 1974, Grogery [23] further investigates and confirms Abramovitz's observation for a six-pad TPTB with 267 mm in OD operating at 4-13 krpm of rotor speed ($\Omega R_m = 40-130$ m/s). To rectify the inconsistency between experiments and theory, Jeng et al. [15] introduce a turbulent flow coefficient ϑ into Ng's model as,

$$\vartheta(Re) = \begin{cases} 0.0 & (Re_h)_{max} \leq Re_L \\ 1.0 - \left(\frac{Re_U - (Re_h)_{max}}{Re_U - Re_L} \right)^{\frac{1}{8}} & Re_L < (Re_h)_{max} \leq Re_U \\ 1.0 & Re_U < (Re_h)_{max} \end{cases} \quad (A.7)$$

where Re_h is the local Reynolds number with an averaged viscosity cross the film. Thus, the fraction $\frac{\epsilon_m}{\nu}$ in Eqn. (A.3) is multiplied by the turbulence coefficient ϑ .

Accordingly, the equivalent turbulent flow viscosity μ^* and heat conductivity κ^* are

$$\mu^*(r, \theta, z) = \mu \left(1 + \vartheta_{(Re)} \frac{\epsilon_m}{\nu} \right) \quad (A.8a)$$

$$\kappa^*(r, \theta, z) = \kappa \left(1 + \vartheta_{(Re)} Pr \frac{\epsilon_H}{\nu} \right) = \kappa \left(1 + \vartheta_{(Re)} \frac{Pr}{Pr^*} \frac{\epsilon_m}{\nu} \right) \quad (A.8b)$$

where the lubricant conductivity κ is constant over the entire film domain and lubricant viscosity (μ) is a function of local temperature (T),

$$\mu = \mu_{Su} e^{-\alpha_{VT}(T-T_{Su})} \quad (A.9)$$

where μ_{Su} and T_{Su} are fluid viscosity and temperature at supply condition and α_{VT} is a fluid temperature-viscosity coefficient.

The Prandtl number Pr and the turbulent Prandtl number Pr^* are,

$$Pr = \frac{\mu C_P}{k} \quad (A.10a)$$

$$Pr^* = \frac{\epsilon_m}{\epsilon_H} \approx 1 \quad (A.10b)$$

and ϵ_H is the eddy viscosity for heat transfer. Note that if the flow is laminar, then $f = 1$, $g = 0$, $\mu^* = \mu$, and $\kappa^* = \kappa$.

B. SHAPE FUNCTIONS FOR AN ANALYTICAL SOLUTION OF PAD ELASTIC DEFORMATIONS

As section 3.4.2 describes, the analytical solution for pad elastic deformations requires a series of shape functions to be defined for deformations over a pad top surface. The shape functions defined in Ref. [8] for spherical pivot (2D tilting) TPTBs are used here,

$$f_1 = \left(\frac{r_c}{r_0}\right)^2 \quad (\text{B.1a})$$

$$f_2 = \left(\frac{r_c}{r_0}\right)^4 \quad (\text{B.1b})$$

$$f_3 = \left(\frac{r_c}{r_0}\right)^2 \sin 2\theta_c \quad (\text{B.1c})$$

$$f_4 = \left(\frac{r_c}{r_0}\right)^2 \cos 2\theta_c \quad (\text{B.1d})$$

$$f_5 = \left(\frac{r_c}{r_0}\right)^4 \sin 2\theta_c \quad (\text{B.1e})$$

$$f_6 = \left(\frac{r_c}{r_0}\right)^4 \cos 2\theta_c \quad (\text{B.1f})$$

The authors also uses additional shape functions for cylindrical pivot (1D tilting) TPTBs,

$$f_1 = \left(\frac{r_c \cos \theta_c}{r_0}\right)^2 \quad (\text{B.2a})$$

$$f_2 = \left(\frac{r_c \cos \theta_c}{r_0}\right)^4 \quad (\text{B.2b})$$

$$f_3 = \left(\frac{r_c \cos \theta_c}{r_0}\right)^2 \sin 2\theta_c \quad (\text{B.2c})$$

$$f_4 = \left(\frac{r_c \cos \theta_c}{r_0}\right)^2 \cos 2\theta_c \quad (\text{B.2d})$$

$$f_5 = \left(\frac{r_c \cos \theta_c}{r_0}\right)^4 \sin 2\theta_c \quad (\text{B.2e})$$

$$f_6 = \left(\frac{r_c \cos \theta_c}{r_0}\right)^4 \cos 2\theta_c \quad (\text{B.2f})$$

where the local cylindrical coordinate (r_c, θ_c) has its origin at the pivot . See Figure 21 for the local coordinate system. Note that all the shape functions are zero at the pivot, some are symmetric around the pivot, and some are unsymmetric. Hence, both symmetrical loading (hydrodynamic pressure) and unsymmetrical loading (temperature gradient) can be represented.

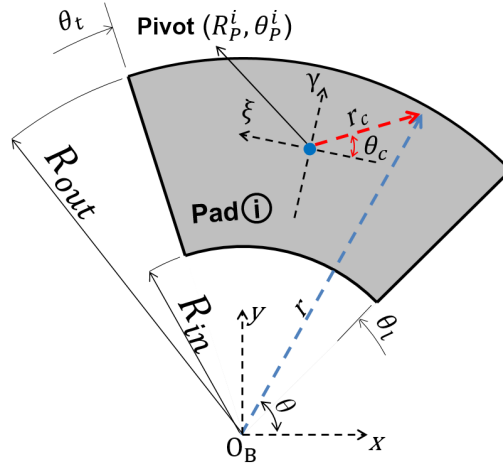


Figure 21: The global (r, θ) and local (r_c, θ_c) cylindrical coordinates systems of a pad.

The relation between the local coordinate and the global coordinate is,

$$r_c = \sqrt{r^2 + R_p^2 - 2rR_p \cos(\theta_p - \theta)} \quad (\text{B.3a})$$

$$\theta_c = \tan^{-1}\left(\frac{r \cos(\theta_p - \theta) - R_p}{r \sin(\theta_p - \theta)}\right) \quad (\text{B.3b})$$

In a cylindrical coordinate, a plate bending energy is,

$$V = \iint_S \frac{Et^3}{24(1-\nu^2)} \left[\left(\frac{\partial^2 w}{\partial r^2} + \frac{1}{r} \frac{\partial w}{\partial r} + \frac{1}{r^2} \frac{\partial^2 w}{\partial \theta^2} \right)^2 - 2(1-\nu) \frac{\partial^2 w}{\partial r^2} \left(\frac{1}{r} \frac{\partial w}{\partial r} + \frac{1}{r^2} \frac{\partial^2 w}{\partial \theta^2} \right) + 2(1-\nu) \left(\frac{\partial}{\partial r} \left(\frac{1}{r} \frac{\partial w}{\partial \theta} \right) \right)^2 \right] dS \quad (\text{B.4})$$

where S is the plate top surface.